Research Article

Photoresponse of Visible Light Active CM-n-TiO$_2$, HM-n-TiO$_2$, CM-n-Fe$_2$O$_3$, and CM-p-WO$_3$ towards Water Splitting Reaction

Yasser A. Shaban[1] and Shahed U. M. Khan[2]

[1] *Department of Marine Chemistry, Faculty of Marine Sciences, King Abdulaziz University, P.O. Box 80207, Jeddah 21589, Saudi Arabia*
[2] *Department of Chemistry and Biochemistry, Duquesne University, Pittsburgh, PA 15282, USA*

Correspondence should be addressed to Shahed U. M. Khan, khan@duq.edu

Photoresponses of visible light active carbon modified titanium oxide (CM-n-TiO$_2$), hydrogen modified titanium oxide (HM-n-TiO$_2$), carbon modified iron oxide (CM-n-Fe$_2$O$_3$), carbon modified tungsten oxide (CM-p-WO$_3$) towards water splitting reaction are reported in this article. Carbon and hydrogen in titanium oxide were found to be responsible for red shift from UV region to visible region which in turn enhanced the photoconversion efficiency by an order of magnitude for water splitting reaction. Photocurrent densities and photoconversion efficiencies of regular n-TiO$_2$ and CM-n-TiO$_2$ towards water splitting reaction under monochromatic light illumination from a xenon lamp and sunlight were compared and found in reasonable agreement. These oxides were characterized by photocurrent measurements, *UV-Vis* spectra, scanning electron microscopy (SEM), energy dispersive x-ray spectroscopy (EDS) and x-ray diffraction (XRD) studies and these results are also reported in this article.

1. Introduction

Sunlight is the unlimited source of clean and renewable energy if it could be efficiently utilized to split water to hydrogen and oxygen. Numerous studies focused on photoelectrochemical water splitting reaction [1–36]. The enhancement of efficiency of a solar hydrogen production process is of considerable importance because high efficiency translates into lower costs. It is, therefore, important to search for a stable and low-cost material for efficiently harvesting the solar energy. To use semiconductors as possible photoelectrodes, their viability depends on their ability to absorb enough sunlight as well as their stability against photocorrosion. The electronic structure of a semiconductor plays a key role in its photoactivity. Unlike a conductor, a semiconductor consists of a valence band (VB) and the conduction band CB). Energy difference between these two levels is said to be the bandgap (E_g) [37].

For efficient H$_2$ production using a visible-light-driven semiconductor (Figure 1), the bandgap should be less than 3.0 eV, but larger than 1.23 eV [38–41]. Moreover, the conduction band (CB) and valence band (VB) levels should satisfy the energy requirements set by the reduction and oxidation potentials for H$_2$O, respectively. For hydrogen production, the CB level should be more negative than hydrogen production level E$_{H_2O/H_2}$ while the VB should be more positive than water oxidation level E$_{H_2O/O_2}$ for efficient oxygen production from water by photocatalysis (Figure 1). Figure 2 shows the bandgap energies; CB and VB positions at pH 2 for different oxide materials that can be used as photoelectrodes. It shows that the CB levels of SrTiO$_3$ and KTaO$_3$ are above H$^+$/H$_2$ but the VB levels of these oxides are below H$_2$O/O$_2$ redox energy level. This means that only the SrTiO$_3$ and KTaO$_3$ can photosplit water without external bias. The TiO$_2$ needs at least 0.3 volt of external bias to photosplit water. However, most of these oxides have very high bandgap energy (>3.1 eV) and hence cannot absorb the visible light of solar spectrum.

1.1. Mechanism of Hydrogen Production from Water. Photoelectrolysis of water in a photoelectrochemical cell (PEC) involves several processes within photoelectrodes and at the photoelectrode/electrolyte interface, including the following.
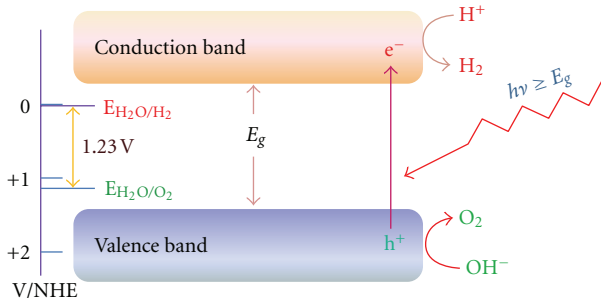
Figure 1: Basic principle of overall water splitting on a cocatalyst-loaded semiconductor.

Autoionization of Water Molecules. In an electrolyte solution, water molecules dissociates into H^+ and OH^-:

$$4H_2O \longrightarrow 4H^+ + 4OH^-. \tag{1}$$

Light-Induced Excitation. When a semiconductor electrode is illuminated by a light source or directly by solar radiation that can provide the electrode with photonic energy ($h\nu$) greater than its bandgap energy (E_g), then an electron from the valence band will be excited into the conduction band, and correspondingly, a positively charged hole will be left in the valence band:

$$\text{photoanode} + \text{sunlight} \longrightarrow 4h^+ + 4e^-. \tag{2}$$
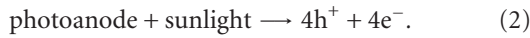
Reduction of Hydrogen Ions. The electrons generated as a result of (2) are transferred over the external circuit to cathode, resulting in the reduction of hydrogen (H^+) ions to gaseous hydrogen:
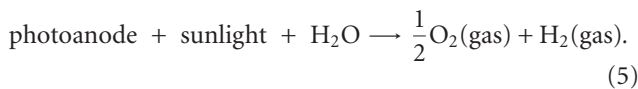
$$4H^+ + 4e^- \longrightarrow 2H_2(\text{gas}) \tag{3}$$
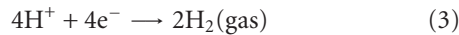
at cathode.

Oxidation of Hydroxyl Ions. The light-induced holes from (2), at the photoanode/electrolyte interface, oxidize the hydroxyl (OH^-) ions to gaseous oxygen as

$$4OH^- + 4h^+ \longrightarrow O_2(\text{gas}) + 2H_2O \tag{4}$$

at photoanode.

The overall reaction will be

$$\text{photoanode} + \text{sunlight} + H_2O \longrightarrow \frac{1}{2}O_2(\text{gas}) + H_2(\text{gas}). \tag{5}$$

1.2. Development of Photoelectrodes for Water Splitting. Among the photoelectrode materials, titanium dioxide (n-TiO_2) was found to be the most promising because of its low cost, chemical inertness, nontoxicity, and photostability. However, its wide bandgap (3.0–3.2 eV) limits its photoresponse in the ultraviolet region which is only a small fraction (~5%) of the sun energy compared to visible light from

400 nm to 750 nm (~49%). Hence, any shift in the optical response of n-TiO_2 from the UV to the visible spectral range will have a profound positive effect on the photocatalytic efficiency of the material. Several attempts were made to lower the bandgap of n-type titanium oxide (n-TiO_2) by transition metal dopants [42, 43] but no noticeable change in bandgap energy of n-TiO_2 was observed. The visible light absorption by the transition metal-doped n-TiO_2 was found to be mainly due to d-d transition of electrons in the transition metal dopants but not due to bandgap lowering. The transition metal dopants acted adversely on photocatalytic activity of n-TiO_2 because they acted as recombination centers for the photogenerated electron-hole pairs.

However, recent studies involved doping of n-TiO_2 by carbon [1, 15–24, 44–49], nitrogen [50, 51], sulphur [52], also fabricating the carbon-modified (CM)-n-TiO_2 in mesoporous [53, 54], and nanostructure [55, 56] forms. Photocatalytic activity of sulphur-doped n-TiO_2 was found to diminish under UV and visible light illuminations due to catalytic poisoning induced by oxidation of sulfur to SO_2 and SO_4^{2-}. Photocatalytic activity of nitrogen-doped n-TiO_2 was reported to be much lower than carbon-doped n-TiO_2 [44].

It was found that carbon modification of n-TiO_2 photocatalyst synthesised by thermal oxidation of Ti metal sheet in a natural gas flame lowered the bandgap energy of n-TiO_2 to 2.32 eV and exhibited water splitting to hydrogen and oxygen with a photoconversion efficiency of 8.35% [1] under artificial light illumination from a Xenon lamp. This progress stimulated further investigation into carbon-modified n-TiO_2 (CM-n-TiO_2) as visible light active photocatalysts [43–49] and also as photoelectrodes [14–24, 55–59] for water-splitting reaction with enhanced photoconversion efficiency. Xu and Khan [16] also showed enhanced rate of water splitting at spray pyrolytically synthesised visible light active carbon-doped n-TiO_2 thin films. Enhanced photoresponse for water splitting at nanocrystalline carbon-doped n-TiO_2 thin films was also reported by Xu et al. [17]. Argon was found to be the most effective calcining ambient to enhance the carbon doping of n-TiO_2 films. The resultant carbon-modified n-TiO_2 thin film calcined in Ar at the optimum temperature of 700°C contained 3.8 at % carbon and showed higher photoresponse in both UV and visible regions compared to those calcined in air at the optimum temperature of 500°C that contained 2.3 at % carbon. Carbon content in these samples calcined in presence of oxygen in air reduced due to removal of some carbon in the forms of CO and CO_2. This wet process synthesis allowed molecular scale mixing of the carbon source with precursor of TiO_2 for improved doping homogeneity and was capable of tuning the carbon content in the film.

Importantly, Mohaputra et al. [18] synthesised CM-n-TiO_2 thin films by flame oxidation of Ti metal sheet and reported photoconversion efficiency of 8.5% for water splitting which is slightly higher than earlier results [1]. Carbon doping was considered to be responsible for the lowering of the bandgap of n-TiO_2 and consequent high photocatalytic activity under visible light illumination. Noworyta and Augustynski [19] observed shift in the spectral response (up to 425 nm) during water-splitting reaction for carbon-doped
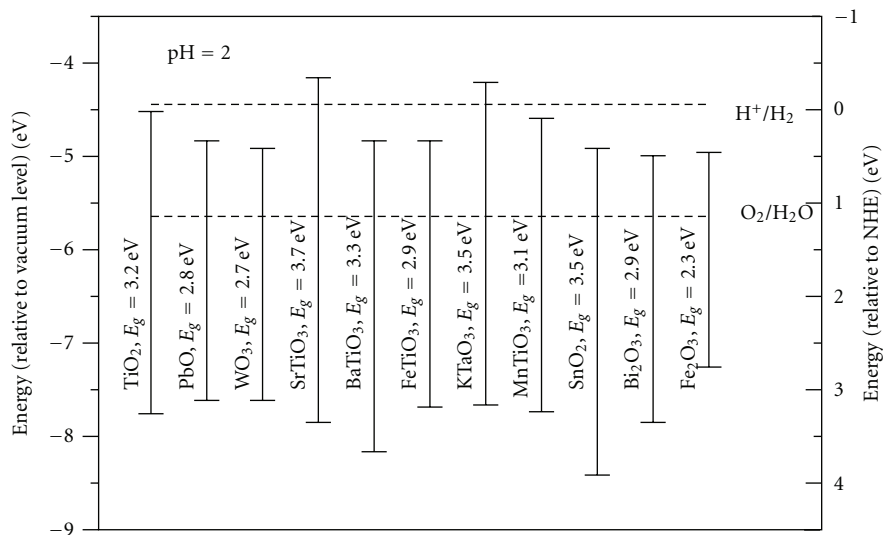
FIGURE 2: Diagram showing bandgap energy of different oxide materials and relative energies in terms of vacuum level and normal hydrogen electrode level in electrolyte of pH = 2 [69].

n-TiO_2 film electrodes formed in the flame of a burner fed with various gas mixtures. Shankar et al. [57] investigated the effect of flame annealing on the spectral photoresponse of titania nanotubes and demonstrated the enhancement of the visible light absorption and the photocurrent for water splitting due to annealing in the flame. However, in their study, the flame annealing was carried out at 1020°C which is much higher than the optimum temperature of 850°C observed earlier [1]. Such high temperature generally removes considerable amounts of carbon from the sample and thus reduces its photoresponse. Given the sensitivity of CM-n-TiO_2 to flame temperature, Shankar et al. [57] and Xu et al. [59] prepared highly ordered n-TiO_2 nanotube arrays by electrochemical anodization of Ti metal sheet followed by calcinations in an electric oven and further oxidation in natural gas flame at optimum temperature to incorporate carbon in it. Significant enhancement of the photoresponse of these carbon-modified (CM) n-TiO_2 nanotube films for water splitting was also reported [58, 59]. Hahn et al. [60] prepared carbon-doped self-organized TiO_2 nanotubes layers formed by electrochemical anodisation of Ti in an HF/Na_2HPO_4 electrolyte. The tubes were treated at 500°C under a mixed flux of N_2 and acetylene (C_2H_2). Nakano et al. [61] prepared TiO_2:C films by oxidative annealing of sputtered TiC films. They reported three bands having energies 0.86 eV, 1.30 eV, and 2.34 eV below the conduction band of carbon-doped n-TiO_2. They attributed the 0.86 eV level to the intrinsic nature of TiO_2, whereas the 1.30 eV and the 2.34 eV levels were newly introduced by C-doping and behaved as deep-level bands. In particular, the pronounced 2.34 eV band contributed to bandgap narrowing by mixing C $2p$ with the O $2p$ valence bands. Therefore, the 2.34 eV level played a significant role for the visible-light sensitivity in TiO_2:C. Ren et al. [62] synthesised a visible light active TiO_2 photocatalyst by carbon doping using glucose as carbon source. The preparation was performed by a hydrothermal method at temperature as low as 160°C. The carbon-doped n-TiO_2 showed absorption in the 400–450 nm range with a red shift in the bandgap transition. Sun et al. [63] reported that carbon-doping-made In_2O_3 red shifted from UV to visible range up to 500 nm and 40% contribution from visible light was observed for the photoelectrochemical splitting of water to hydrogen. Cardenas et al. [64] reported marked decrease in resistivity of carbon-doped antimony sulfide (Sb_2S_3) thin films to 102 Ω cm compared to 108 Ω cm for undoped samples, and electrical resistivity was also possible to tune by controlling the carbon content (wt %) in the sample. The bandgap energy the carbon-doped Sb_2S_3 thin films was found to decrease to 1.7 eV from 2.57 eV for undoped sample. This result indicates that carbon doping of Sb_2S_3 is not only capable of bandgap lowering but can also enhance the conductivity of the sample.

In an important theoretical study, Nie and Sohlberg [65] reported the lowering of the bandgap of n-TiO_2 to 2.32 eV (535 nm) due to carbon incorporation and predicted that the bandgap value of 1.58 eV may be possible to achieve by some complex carbon incorporation. Interestingly, it was found experimentally that enhanced carbon doping lowered the bandgap of n-TiO_2 up to 1.45 eV [16]. Wang and Lewis [66, 67] addressed theoretically the effects of carbon dopants concentration on the photoresponse of n-TiO_2 in the visible-light region. They found that the substitutional and interstitial carbon dopants incorporated into TiO_2 drastically affected the electronic structure of the material, thus improving its photoactivity. They predicted the low bandgap of 2.35 eV for carbon-doped TiO_2 as it was experimentally observed earlier [1]. The theoretical findings of Di Valentin et al. [68] revealed the presence of substitutional and interstitial carbon in carbon-modified (CM)-n-TiO_2 (Figure 3) which were found to be responsible for the lowering of its main bandgap as well as generating a mid-gap band.

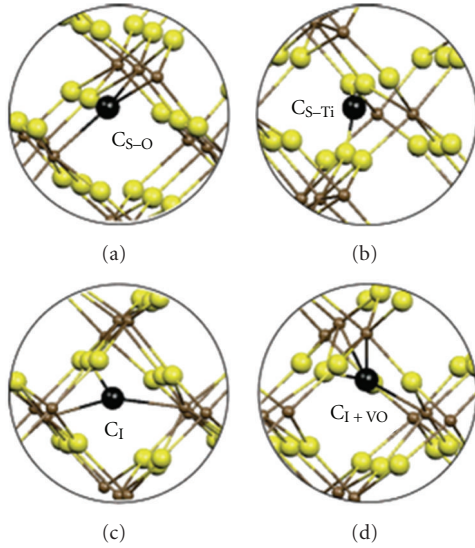Figure 3: Partial geometry of the models for (a) one substitutional C atom to O (C_{S-O}), (b) one substitutional C atom to Ti (C_{S-Ti}), (c) one interstitial C atom (C_I), and (d) one interstitial C atom nearby an oxygen vacancy (C_{I+VO}) in the rutile supercell. The yellow spheres represent O atoms, the small brown spheres represent Ti atoms, and the black sphere presents the carbon impurity [68].

Among various oxide semiconductor photocatalysts, iron (III) oxide (Fe_2O_3) is a low-cost semiconductor with high stability. Iron (III) oxide has a bandgap of 2.0–2.3 eV; therefore, it can absorb solar radiation up to 620 nm, which covers ~37% of the photons of the solar spectrum of global AM 1.5 (1 sun) [70]. However, challenges are set by its quite low photoresponse due to its high resistivity and consequent recombination of photogenerated carriers. To minimise these limitations, it has been reported that dopants, either n-type [4, 7, 26, 27] or p-type [28–30], improved the photoresponse of iron (III) oxide (Fe_2O_3) towards water splitting to hydrogen. Thin films of n-Fe_2O_3 were extensively studied [4, 7, 25–36]. For example, n-Fe_2O_3 films were synthesised by a sputtering method [30], by pressing powders of Fe_2O_3 [32–34], and by spray pyrolysis method [4, 7, 28–30, 32]. Silicon-doped Fe_2O_3 films synthesised by ultrasonic spray pyrolysis showed $1.0 \, \text{mA cm}^{-2}$ at +0.1 V versus AgCl [36] under solar-simulated light illumination at 1 sun, AM 1.5 ($100 \, \text{mW cm}^{-2}$).

Tungsten trioxide (WO_3) is also of great interest and has been investigated extensively due to its promising physical and chemical properties [70–73] The WO_3 films are nontoxic and have relatively low price. Semiconducting tungsten oxide (WO_3) is an interesting candidate for photocataylsis because of its relatively low bandgap energy (E_g = 2.6 eV), [74–76] resulting in possible utilization of 12% of the solar spectrum [77]. Spectral response studies were carried out for n-type WO_3 by different workers [78, 79]. For example, n-WO_3 films were synthesized by conventional evaporation techniques [80, 81] and, more recently, with the sol-gel process [82, 83]. It is important to note that regular undoped tungsten oxide is an n-type semiconductor, but when it

is carbon-doped or carbon-modified, it was found to be a p-type tungsten oxide. Carbon-modified p-type tungsten oxide (CM-p-WO_3) films were synthesized by thermal flame oxidation method at several flame temperatures for different lengths of time [84].

In this paper, we summarize our studies on thin-film photoelectrodes of the following

 (i) visible light active carbon-modified titanium oxides (CM-n-TiO_2);

 (ii) visible light active hydrogen modified n-type titanium oxide (HM-n-TiO_2) thin films;

 (iii) carbon-modified iron oxides (CM-n-Fe_2O_3) thin films;

 (iv) visible light active carbon-modified p-type tungsten oxides (CM-p-WO_3) thin film.

The results of photocurrent density measurements on these photoelectrodes for water splitting to H_2 and O_2 and the maximum photoconversion efficiencies under both Xenon lamp and natural sunlight of global AM 1.5 illuminations are also provided. Synthesized thin-film photoelectrodes are characterized in terms of bandgap energies, X-ray diffraction pattern, scanning electron micrograms, and carbon contents to correlate with their photoresponse towards water-splitting reaction.

2. Experimental Details and Results

2.1. Visible Light Active Carbon-Modified Titanium Oxides (CM-n-TiO_2) Thin Films.
Shaban and Khan [23] synthesized visible light active carbon-modified n-type titanium oxide (CM-n-TiO_2) thin films by flame oxidation of Ti metal sheets both flat and grooved and also by using combination of spray pyrolysis and flame oxidation methods. Also undoped reference n-TiO_2 samples were synthesized in an electric oven for comparison. The flame was custom designed by Knight Co. The flame temperature was controlled by adjusting the flow rates of oxygen and natural gas.

2.1.1. Dependence of Photocurrent Density on Measured Electrode Potential for Titanium Oxides.
Plots of photocurrent density (j_p, mA cm^{-2}) as a function of measured potential, E_{meas} (V/SCE) for oven-made n-TiO_2 synthesized at 825°C for 16 min (sample 1); CM-n-TiO_2 synthesized by only thermal flame oxidation of Ti at 825°C for 16 min (sample 2); grooved CM-n-TiO_2 synthesized by only thermal flame oxidation of Ti (0.005 inch groove depth) at 820°C for 18 min (sample 3); CM-n-TiO_2 synthesized by spray pyrolysis of 0.175 M $TiCl_4$ in ethanol at substrate temperature of 460°C for 20 sec at carrier gas (oxygen) pressure of 20 psi followed by thermal flame oxidation at 825°C for 16 min (sample 4) are shown in Figure 4. Sample 1 shows the lowest photocurrent density of $1.6 \, \text{mA cm}^{-2}$ measured at –0.4 V/SCE. The observed low photocurrent density for sample 1 was due to absence of carbon as well as lower thickness in such electric oven-made samples. Sample 4 generated the highest photoresponse compared to samples, 1, 2, and 3.
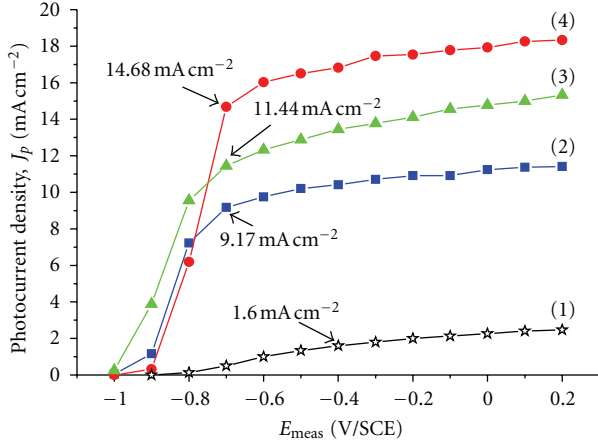
FIGURE 4: Photocurrent density, j_p (measured under light intensity of $100\,mW\,cm^{-2}$ from a 150 Watt Xenon lamp) as a function of measured potential, E_{meas} (V/SCE), for oven-made n-TiO$_2$ synthesized at $825°C$ for 16 min (sample 1); CM-n-TiO$_2$ synthesized by only thermal flame oxidation of Ti at $825°C$ for 16 min (sample 2); grooved CM-n-TiO$_2$ synthesized by only thermal flame oxidation of Ti (0.005 in groove depth) at $820°C$ for 18 min (sample 3); CM-n-TiO$_2$ synthesized by spray pyrolysis of 0.175 M TiCl$_4$ in ethanol at substrate temperature of $460°C$ for 20 sec at carrier gas (oxygen) pressure of 20 psi followed by thermal flame oxidation at $825°C$ for 16 min (sample 4); electrolyte solution of 5 M KOH was used. The electrode potentials at open circuit condition under illumination, E_{aoc}, were found to be -0.977 V/SCE (sample 1), -0.940 V/SCE (sample 2), -0.942 V/SCE (sample 3), and -0.915 V/SCE (sample 4) [21–23].

Photocurrent density, measured at -0.7 V/SCE, increased significantly from $9.17\,mA\,cm^{-2}$ for sample 2 to $11.44\,mA\,cm^{-2}$ for sample 3. The surface grooving of Ti metal increased the effective surface area of oxide layer in sample 3 and consequently generated higher photocurrent density. A sharp increase in photocurrent density to $14.68\,mA\,cm^{-2}$ measured at -0.7 V/SCE for sample 4 can be attributed to increased thickness of the oxide layer synthesized by combination of spray pyrolysis and flame oxidation methods. This is because increased thickness allows absorption of more light to generate more electron-hole pairs (excitons).

2.1.2. Dependence of Photoconversion Efficiency on Applied Potential for CM-n-TiO$_2$ Films. The calculation of total percent photoconversion efficiency (%ε_{photo}(total)) of light energy under white light illumination to chemical energy in the presence of an external applied potential (E_{app}) was carried out using the equation given earlier [1, 4] as

$$\%\varepsilon_{photo}(total) = \frac{j_p\left[E_{rev}^o - \left|E_{app}\right|\right]}{P_o} \times 100, \qquad (6)$$

where j_p is the photocurrent density (mA cm^{-2}), E_{rev}^o is the standard reversible potential (which is 1.23 V for water splitting reaction), P_o is the power density of incident light

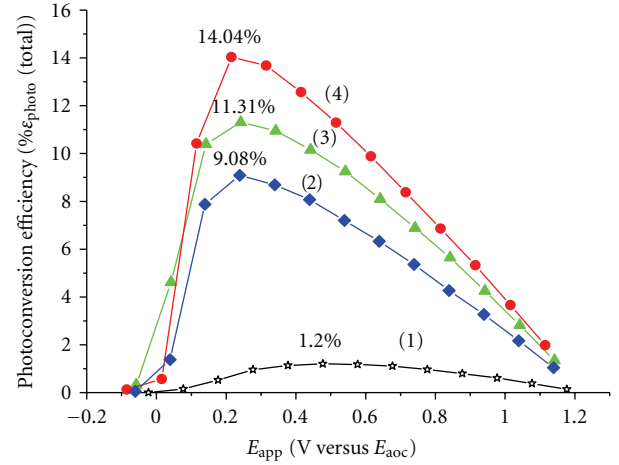FIGURE 5: Dependence of photoconversion efficiency, %ε_{photo}(total), on applied potential E_{app} (V versus E_{aoc}), for samples 1, 2, 3, and 4 [21–23].

(mW cm^{-2}), $|E_{app}|$ is the absolute value of the applied potential which is obtained as [1]

$$E_{app} = (E_{meas} - E_{aoc}), \qquad (7)$$

where E_{meas} (versus SCE) is the potential at which the photocurrent density was measured, E_{aoc} (versus SCE) is the electrode potential at open circuit condition in the same electrolyte solution under the same illumination intensity at which the photocurrent density was measured. The values of E_{aoc} (versus SCE) were found to be -0.847 V, -0.940 V, -0.942 V, -0.915 V for samples 1, 2, 3, and 4, respectively.

The corresponding maximum photoconversion efficiencies (see Figure 5) were found to be 1.2% at 0.447 V bias, 9.08% at 0.240 V bias, 11.31% at 0.242 V bias, and 14.04% at 0.215 V bias for samples 1, 2, 3, and 4, respectively, under illumination intensity of $100\,mW\,cm^{-2}cm^{-2}$ from a 150 watt Xenon lamp.

2.1.3. Monochromatic Photocurrent Density-Wavelength Dependence for CM-n-TiO$_2$ Films. The plots of monochromatic photocurrent density, $j_p(\lambda)$, as a function of wavelength of light, λ, for samples 1, 2, 3, and 4 are shown in Figure 6. The monochromatic photocurrent density, $j_p(\lambda)$, was measured at measured potentials corresponding to applied potential at which maximum %ε_{photo}(total) was observed (see Figure 5) under white light illumination. The values of E_{app} used were 0.477 V, 0.240 V 0.242 V, and 0.215 V for samples 1, 2, 3, and 4, respectively. Performing integration under the curve, total photocurrent densities of $1.25\,mA\,cm^{-2}$, $8.95\,mA\,cm^{-2}$, $11.30\,mA\,cm^{-2}$, and $13.58\,mA\,cm^{-2}$ were found for samples 1, 2, 3, and 4, respectively. These values are a little lower than the corresponding photocurrent density values under white light illumination from the Xenon lamp because of loss of some light passing through the monochromator.

Note that the observed photocurrent in the visible region for the CM-TiO$_2$ samples cannot be due to artifact of

(1) J_p flat by oven = 1.25 mA cm^{-2}
(2) J_p flat by flame = 8.95 mA cm^{-2}
(3) J_p grooved by flame = 11.3 mA cm^{-2}
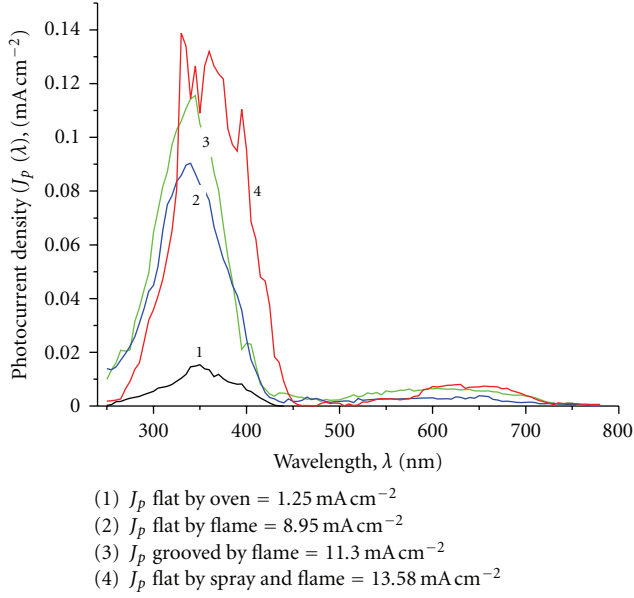(4) J_p flat by spray and flame = 13.58 mA cm^{-2}

FIGURE 6: The monochromatic photocurrent density, $j_p(\lambda)$, as a function of wavelength of light, λ, for samples 1, 2, 3, and 4, respectively [21–23].

(1) %ε_{photo} (total) flat by oven = 0.94%
(2) %ε_{photo} (total) flat by flame = 8.86%
(3) %ε_{photo} (total) grooved by flame = 11.16%
(4) %ε_{photo} (total) flat by spray and flame = 13.79%

FIGURE 7: The photoconversion efficiency, %$\varepsilon_{photo}(\lambda)$, as a function of wavelength of light, λ, for samples 1, 2, 3, and 4 [21–23].

a monochromator or due to second harmonic generation because if that would be the case the regular n-TiO$_2$ would have shown photocurrent in the visible region. Figure 6 clearly shows no photocurrent for regular n-TiO$_2$ in the wavelength region between 500 nm 750 nm. Recent combined sputtering and XPS studies showed that carbon incorporation was limited to few angstroms (15 Å to 20 Å) deep. Hence, the amounts of visible light absorption were low as demonstrated by low photocurrent in the visible region between 500 nm to 750 nm (see Figure 6).

2.1.4. Photoconversion Efficiency from Monochromatic Photocurrent Density for CM-n-TiO$_2$ Films.
Alternatively, the percent total photoconversion efficiency (%ε_{photo}(total)) of light energy to chemical energy can be obtained by using the following equation [20, 21, 68, 70]:

$$\%\varepsilon_{photo}(\text{total}) = \frac{\int_{\lambda_{min}}^{\lambda_g} j_p(\lambda)\left[E_{rev}^o - \left|E_{app}(\lambda)\right|\right]d\lambda}{\int_{\lambda_{min}}^{\infty} P_o(\lambda)d\lambda} \times 100, \quad (8)$$

where $j_p(\lambda)$ is wavelength-dependent photocurrent density under monochromatic light illumination (mA cm^{-2} nm^{-1}) and $P_o(\lambda)$ is the power density of incident wavelength-dependent monochromatic light (mW cm^{-2} nm^{-1}). Note that the applied potential, $E_{app}(\lambda)$, was also found to be wavelength-dependent and can be expressed as

$$E_{app}(\lambda) = E_{meas} - E_{aoc}(\lambda), \quad (9)$$

where $E_{aoc}(\lambda)$ is the electrode potential in volts at open-circuit conditions under monochromatic light illumination. However, λ_{min} = 250 nm for light from Xenon lamp and

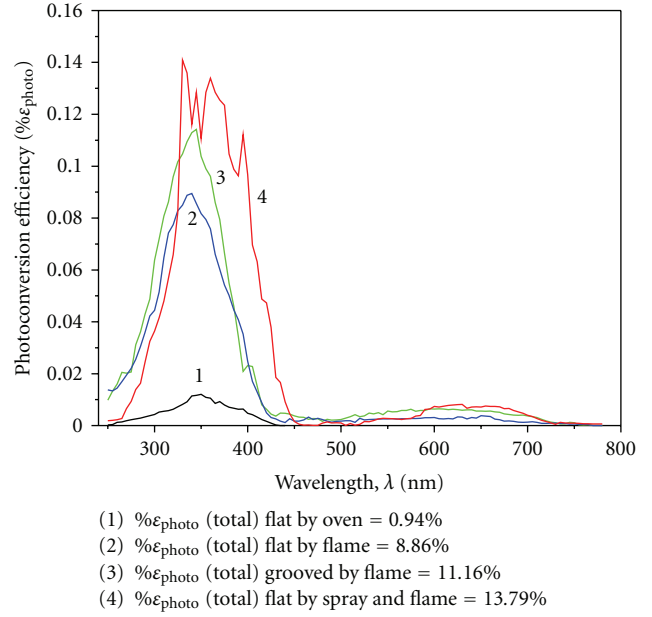300 nm for sunlight were used, and $\lambda_g = 1239.85/E_g$ is the threshold wavelength corresponding to bandgap energy, E_g, of the sample in electron volt unit.

Note that wavelength-dependent percent photoconversion efficiency, %$\varepsilon_{photo}(\lambda)$ can be expressed as [20, 21],

$$\%\varepsilon_{photo}(\lambda) = \frac{j_p(\lambda)\left[E_{rev}^o - \left|E_{app}(\lambda)\right|\right]}{\int_{\lambda_{min}}^{\lambda_{max}} P_o(\lambda)d\lambda} \times 100. \quad (10)$$

The plot of %$\varepsilon_{photo}(\lambda)$ versus wavelength, λ, using (10) is given in Figure 7 where total intensity in the denominator of (10) was taken as 100 mW cm^{-2}. Performing the integration (as given in (8)) from λ_{min} = 250 nm (for Xenon lamp white light) to λ_g nm or determining the area under the curve in Figure 7 obtained using (10), the total photoconversion efficiencies of 0.94%, 8.86%, 11.16%, and 13.79% were obtained for samples 1, 2, 3, and 4, respectively. Note that λ_{max} represents the maximum wavelength available in sunlight which is 4200 nm. These values are little lower but comparable to 1.2%, 9.08%, 11.31%, and 14.04% (when calculated using (6) under white light illumination of intensity 100 mW cm^{-2} from a 150 W Xenon lamp) for samples 1, 2, 3, and 4, respectively. These lower values can be attributed to loss of some light through the monochromator as well as the use of average value of $E_{app}(\lambda)$ instead of using its experimentally determined value at each wavelength, λ.

2.1.5. Bandgap Energy Determination for n-TiO$_2$ and CM-n-TiO$_2$ Films.
The bandgap energy, E_g, can be determined from the frequency of light, ν, dependent quantum efficiency, $\eta(\nu)$, using the following equation [4, 5, 7]:
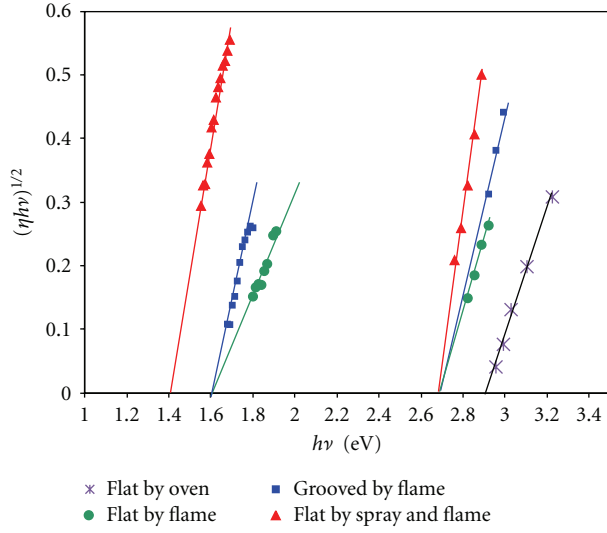
$$\eta(\nu)h\nu = A\left(h\nu - E_g\right)^n, \quad (11)$$

FIGURE 8: The respective plots of $[\eta(\lambda)h\nu]^{1/2}$ versus $h\nu$ to determine the bandgap for samples 1, 2, 3, and 4 [21–23].
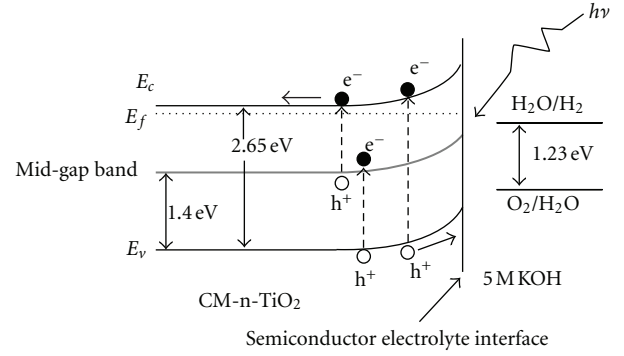

FIGURE 9: A schematic diagram of valence, conduction, and mid-gap bands to show the bandgaps in CM-n-TiO$_2$ films synthesized by thermal flame oxidation of Ti metal sheet [21–23].

where A is a constant, n equals either 0.5 for allowed direct transition or 2 for allowed indirect transitions, $h\nu$ is the photon energy of frequency ν. The wavelength, λ, dependent quantum efficiency, $\eta(\lambda)$, or incident photon conversion efficiency, IPCE(λ), can be expressed as [20, 21]

$$
\begin{aligned}
\eta(\lambda) = \text{IPCE}(\lambda) &= \frac{j_p(\lambda)}{[eI_o(\lambda)]} \\
&= \frac{\left[1239.85(\text{Vnm})j_p(\lambda)(\text{mA cm}^{-2}\text{nm}^{-1})\right]}{[\lambda(\text{nm})P_o(\lambda)(\text{mW cm}^{-2}\text{nm}^{-1})]},
\end{aligned}
\tag{12}
$$

where e is the electronic charge and the incident photon flux, and the wavelength-dependent photon flux, $I_o(\lambda)$, (cm^{-2} nm^{-1} s^{-1}) was expressed as [20, 21]

$$
\begin{aligned}
I_o(\lambda) &= P_o(\lambda)\frac{\lambda}{hc} \\
I_o(\lambda) &= \frac{[P_o(\lambda)(\text{mW cm}^{-2}\text{nm}^{-1})\lambda(\text{nm})]}{[1239.85(\text{V nm})e]},
\end{aligned}
\tag{13}
$$

where h is the Planck's constant and c is the velocity of light.

Figure 8 shows $[\eta(\lambda)h\nu]^{1/2}$ versus $h\nu$ plot for samples 1, 2, 3, and 4, respectively. From the intercepts of the straight lines the bandgaps were obtained. It shows two indirect bandgap energies for all CM-n-TiO$_2$ photoelectrodes. The first bandgap energy of 2.65 eV corresponds to lowering of original bandgap (samples 2, 3, and 4) and second bandgap with values of 1.6 eV and 1.4 eV can be attributed to mid-gap band generated by carbon doping as shown in the schematic diagram in Figure 9. Theoretical analysis [65, 66, 70] and experimental findings [20, 21] also showed multiple bandgaps in CM-n-TiO$_2$. Oven-made n-TiO$_2$ showed only one bandgap of 2.9 eV, and as a result, poor photoresponse was obtained. Note that the first bandgap energy values for all CM-n-TiO$_2$ samples were found equal. The slopes of bandgap plots for sample 4 were found to be the

highest, which is in accordance with the highest observed photoresponse generated by this sample.

2.1.6. Spectral Distribution of Light for Global AM 1.5 Natural Sunlight (1 Sun) and Xenon Lamp Light (100 mW cm^{-2}). It is important to compare the spectral distribution of light from both Xenon lamp and sunlight. Figure 10 compares the spectral distribution of these two lights. The integrated value of the intensity from 300 up to 800 nm for global sunlight AM 1.5 (1 sun = 100 mW cm^{-2} measured by NREL [85]) was found to be 59.00 mW cm^{-2} clearly indicating that the contribution from remaining light from 800 nm to 4100 nm present in global sunlight will be 41.00 mW cm^{-2} [= (100–59) mW cm^{-2}]. Hence, total Xenon lamp light comparable to sunlight (1sun) will be 98 mW cm^{-2} [= (57 + 41) mW cm^{-2}] where 57.00 mW cm^{-2} is the integrated value of intensity from 200 nm to 800 nm for Xenon lamp light.

Note that the spectral distribution of Xenon lamp light begins below 250 nm compared to global AM 1.5 sunlight that begins at 300 nm. Furthermore, the spectral distribution of Xenon lamp light is higher in the UV region, but in the visible region, it is lower than that of sunlight. Hence, one will expect comparable photocurrent density and photoconversion efficiencies for CM-n-TiO$_2$ samples for water splitting under actual global sunlight illumination of AM 1.5 (1 sun) and the Xenon lamp illumination of intensity of 100 mW cm^{-2}. However, relatively higher values for photocurrent density and photoconversion efficiency under Xenon lamp illumination will be expected compared to those under sunlight for CM-TiO$_2$ due to higher spectral distribution of the former in the UV region than in the visible region (see Figure 10) and that the absorption coefficient of light for CM-TiO$_2$ in UV region is much higher compared to that in the visible region. Also, only 1.5 to 2.0 nm deep carbon modified region in CM-n-TiO$_2$ could not absorb enough light in the visible region.

2.1.7. Photocurrent Density and Photoconversion Efficiency for Titanium Oxides from IPCE(λ) Using Illumination Intensity, $I_o(\lambda)$ of Natural Global AM 1.5 Sunlight. Utilizing the values of the wavelength-dependent incident photon conversion
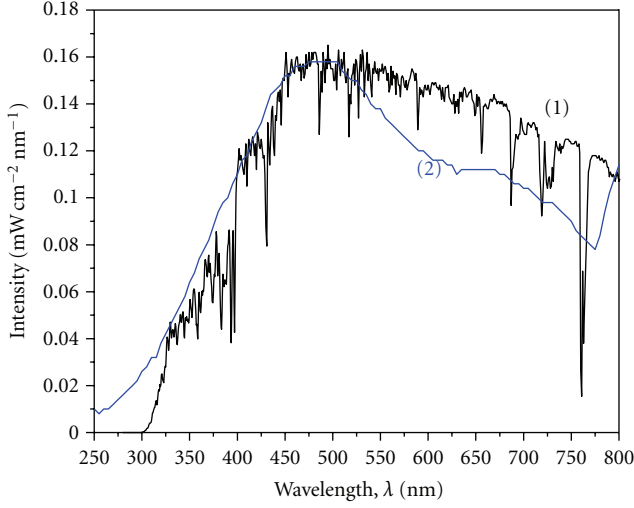
(1) Global AM 1.5
(2) Xenon lamp

FIGURE 10: The wavelength-dependent intensity of light from a 150 W Xenon lamp at intensity of $100\,\mathrm{mW\,cm^{-2}}$, measured by using silicon photon detector (UDT Sensors. Inc., Model 10DP/SB), compared to the wavelength-dependent intensity of natural global AM 1.5 sunlight in the wavelength range from 300 to 800 nm obtained from NREL website [85].

efficiency IPCE (λ) or quantum efficiency $\eta(\lambda)$ of these samples, it is possible to determine the photocurrent density, $j_p^{\mathrm{sunlight}}(\lambda)$, under natural global AM 1.5 sunlight illumination as [20, 21]

$$j_p^{\mathrm{sunlight}}(\lambda) = \mathrm{IPCE}(\lambda)eI_o^{\mathrm{sunlight}}(\lambda), \qquad (14)$$

where $I_o^{\mathrm{sunlight}}(\lambda)$ is the wavelength-dependent photon flux of incident global AM 1.5 sunlight which can be obtained using (13) in which photon power density of sunlight $P_o^{\mathrm{sunlight}}(\lambda)$ was used from the tabulated data given in National Renewable Energy Laboratory (NREL) website [85].
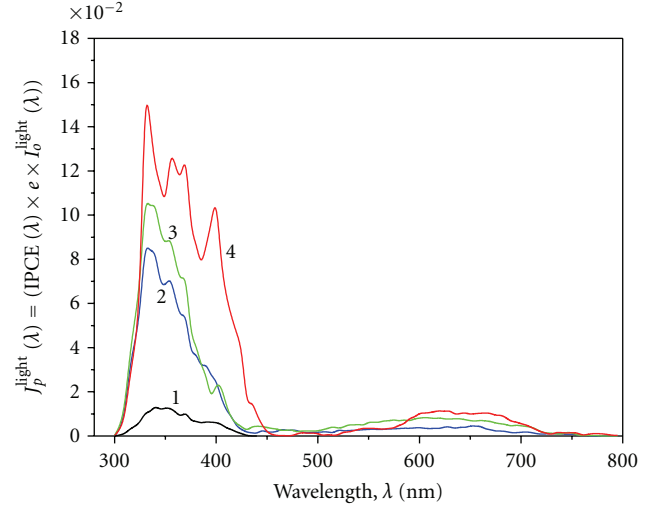
The plots of $j_p^{\mathrm{sunlight}}(\lambda)$ [data obtained from (14)] versus the wavelength of light, λ, for samples 1–4 are given in Figure 11. The integrated values of total current density under sunlight illumination were found to be 0.85 mA $\mathrm{cm^{-2}}$, 5.89 mA $\mathrm{cm^{-2}}$, 7.71 mA $\mathrm{cm^{-2}}$, and 12.27 mA $\mathrm{cm^{-2}}$ for sample 1, 2, 3, and 4, respectively.

The total photocurrent density, $j_p^{\mathrm{sunlight}}(\mathrm{total})$, under sunlight illumination can be expressed as [20, 21]

$$j_p^{\mathrm{sunlight}}(\mathrm{total}) = e \int_{\lambda\,\mathrm{min}}^{\lambda_{\mathrm{g}}} \mathrm{IPCE}(\lambda)I_o(\lambda)d\lambda. \qquad (15)$$

The total photoconversion efficiency under natural sunlight illumination can be expressed as [20, 21]

$$\%\varepsilon_{\mathrm{solar}}^{\mathrm{sunlight}}(\mathrm{total}) = \frac{\int_{\lambda_{\mathrm{min}}}^{\lambda_{\mathrm{g}}} j_p^{\mathrm{sunlight}}(\lambda)\left[E_{\mathrm{rev}}^o - \left|E_{\mathrm{app}}(\lambda)\right|\right]d\lambda}{\int_{\lambda_{\mathrm{min}}}^{\lambda\,\mathrm{max}} P_o^{\mathrm{sunlight}}(\lambda)d\lambda}$$

$$\times\,100, \qquad (16)$$

(1) J_p^{sunlight} flat by oven = $0.85\,\mathrm{mA\,cm^{-2}}$
(2) J_p^{sunlight} flat by flame = $5.89\,\mathrm{mA\,cm^{-2}}$
(3) J_p^{sunlight} grooved by flame = $7.71\,\mathrm{mA\,cm^{-2}}$
(4) J_p^{sunlight} flat by spray and flame = $12.27\,\mathrm{mA\,cm^{-2}}$

FIGURE 11: Wavelength-dependent photocurrent density under global sunlight illumination, $j_p^{\mathrm{sunlight}}(\lambda) = [\mathrm{IPCE}(\lambda) \times e \times$ global sunlight intensity, $I_o^{\mathrm{sunlight}}(\lambda)]$, versus wavelength, λ of incident sunlight for samples 1, 2, 3, and 4 (14) [23].

where the denominator was taken as $100\,\mathrm{mW\,cm^{-2}}$ for actual natural global AM 1.5 sunlight (1 sun).

Hence, using (15) and the denominator in (16) as $100\,\mathrm{mW\,cm^{-2}}$ for global AM 1.5 sunlight, one can express the simplified form of (16) as

$$\%\varepsilon_{\mathrm{solar}}^{\mathrm{sunlight}}(\lambda)$$

$$= \frac{j_p^{\mathrm{sunlight}}(\lambda)\,\mathrm{mA\,cm^{-2}}\left[1.23 - \left|E_{\mathrm{app}}\right|_{\mathrm{average}}\mathrm{volt}\right]}{100\,\mathrm{mW\,cm^{-2}}}$$

$$\times\,100, \qquad (17)$$

$$\%\varepsilon_{\mathrm{solar}}^{\mathrm{sunlight}}(\mathrm{total})$$

$$= \frac{j_p^{\mathrm{sunlight}}(\mathrm{total})\,\mathrm{mA\,cm^{-2}}\left[1.23 - \left|E_{\mathrm{app}}\right|_{\mathrm{average}}\mathrm{volt}\right]}{100\,\mathrm{mW\,cm^{-2}}}$$

$$\times\,100, \qquad (18)$$

where $E_{\mathrm{rev}}^o = 1.23$ volt was used for water-splitting reaction and an average value of the absolute value of applied potential, $|E_{\mathrm{app}}|_{\mathrm{average}}$, was used for all wavelength, λ values.

Photoconversion efficiencies under sunlight illumination were obtained using (16) or (18). Figure 12 shows the calculated wavelength-dependent percent photoconversion efficiencies under sunlight illumination, $\%\varepsilon_{\mathrm{solar}}^{\mathrm{sunlight}}(\lambda)$, as a function of wavelength of incident light λ using (17).
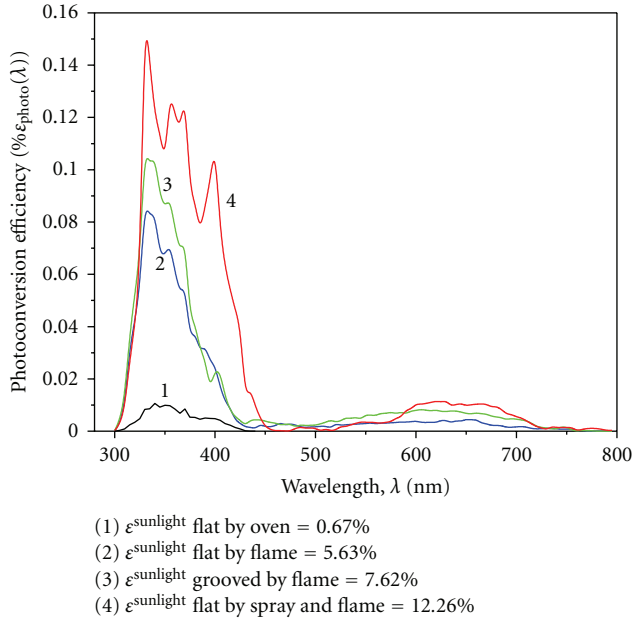
FIGURE 12: Wavelength-dependent photoconversion efficiency under sunlight illumination, $\%\varepsilon_{solar}^{sunlight}(\lambda)$, versus wavelength, λ of incident light for samples 1, 2, 3, and 4 (17) [21–23].

(1) $\varepsilon^{sunlight}$ flat by oven = 0.67%
(2) $\varepsilon^{sunlight}$ flat by flame = 5.63%
(3) $\varepsilon^{sunlight}$ grooved by flame = 7.62%
(4) $\varepsilon^{sunlight}$ flat by spray and flame = 12.26%

(1) Flat by oven (ε_{photo} (total) = 1.2%)
(2) Flat by flame (ε_{photo} (total) = 9.08%)
(3) Grooved by flame (ε_{photo} (total) = 11.31%)
(4) Flat by spray and flame (ε_{photo} (total) = 14.04%)

FIGURE 13: UV-Vis Spectra of titanium oxides (samples 1–4) [21–23].

Performing the integration under the curve from 300 nm to λ_g, photoconversion efficiencies of 0.67%, 5.63%, 7.62, and 12.26% were found for samples 1, 2, 3, and 4, respectively. These results indicate that CM-n-TiO$_2$ thin films synthesized by combination of spray pyrolysis and natural gas flame oxidation (sample 4) can be expected to split water with ≥10% even under actual sunlight illumination. The photoconversion efficiency values for these 4 samples under different illumination conditions are summarized in Table 1.

2.1.8. UV-Vis Spectra of n-TiO$_2$ and CM-n-TiO$_2$ Films. The UV-Vis absorbance of n-TiO$_2$ and CM-n-TiO$_2$ photoelectrodes is shown in Figure 13. The absorption spectra of CM-n-TiO$_2$ samples 1, 2, 3, and 4 demonstrate a wide absorption in the UV and visible regions with a tail extending to near infrared region up to 800 nm. This indicates low bandgap energy values for these samples. The reference oven-made n-TiO$_2$ (sample 1) shows absorption only up to 415 nm which corresponds to bandgap energy of 3.0 eV. The lower bandgaps of CM-n-TiO$_2$ samples may be due to carbon incorporation during the flame oxidation of Ti metal sheet. Note that carbon modification also generates oxygen vacancy by partial reduction of TiO$_2$ and this intern may be partially responsible for visible light activity of carbon-modified titanium oxide (CM-n-TiO2). The UV-Vis spectroscopic results show higher absorption in UV as well as in the visible regions for CM-n-TiO$_2$ films synthesized by combination of spray pyrolysis and flame oxidation (sample 3) compared to sample 2. Also, these UV-Vis spectra are consistent with the higher photocurrent densities at CM-n-TiO$_2$ thin-film electrodes prepared by the combination of two methods. Importantly, this observation conforms to
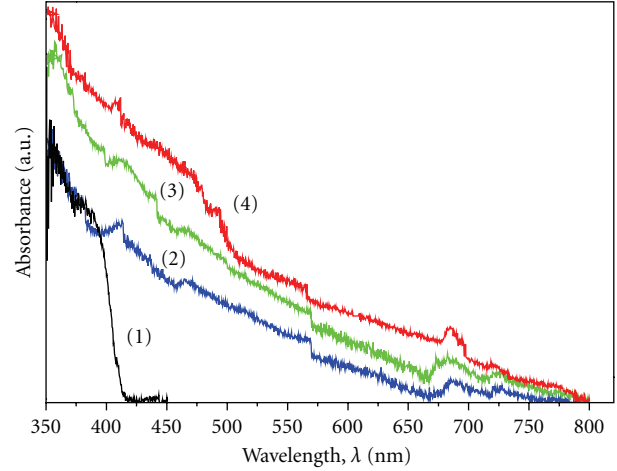
the important hypothesis that the spray pyrolysis increased the thickness of the visible light active CM-n-TiO$_2$ films. Consequently, these films absorbed more light.

However, the UV-Vis spectra (see Figure 13) do not match well with the monochromatic photocurrent density-wavelength dependence (see Figure 6). The UV-Vis spectra represent the excitation of electron from lower energy state (to generate holes in this state) to higher energy state by absorption of light. However, to have observed photocurrent, photogenerated holes will have to (1) transport to the interface and (2) undergo transition across the interface to available (thermally distributed) hole acceptor states (e.g., OH$^-$) in solution. These two extra processes are responsible not having UV-Vis spectra to match with the monochromatic photocurrent density-wavelength-dependent plots.

The electrons that are excited to conduction band from the shallow mid-gap states in CM-n-TiO$_2$ (see Figure 9) by light of around 500 nm reasonable amount of absorption were observed in the UV-Vis spectra but the holes generated in the mid gap band (see Figure 9) were lost due to very low availability of acceptor states of holes in solution (e.g., OH$^-$ ion) and consequently generated negligible photocurrent density (see Figure 6). However, absorption in UV-Vis spectra around 500 nm is observed since such absorption does not need availability of acceptor state of holes in solution. Furthermore, the light around 500 nm (2.48 eV) having sub-bandgap energy cannot be absorbed by CM-n-TiO$_2$ to generate electron-hole pairs in its valence band. However, the light around 600 nm to 700 nm can excite electrons from the valence band to mid-gap band states of CM-n-TiO$_2$ (see Figure 9) and these electrons move to the counter electrode. The corresponding holes generated in the valence band undergo transition to available hole acceptor states in solution. Consequently, some photocurrents are observed

TABLE 1: Maximum photoconversion efficiencies (%) under Xenon lamp light and actual natural sunlight illumination conditions for reference electric oven-made (n-TiO$_2$), flame-made, and spray-flame-made CM-n-TiO$_2$ samples and their bandgap and mid-gap Energies [21–23].

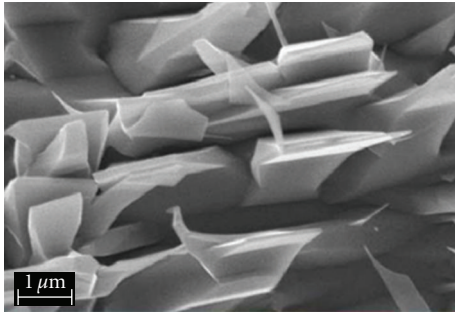| Titanium Oxide,TiO$_2$ samples | %ε_{photo}(total) | | | | Bandgap energies | |
| | Under white light illumination from Xenon lamp light | Under monochromatic light illuminations from Xenon lamp | | Under monochromatic actual natural sunlight illuminations (integrated from 300 nm present in sunlight) | Bandgap energy (eV) | Mid-gap energy (eV) |
		Integrated from 250 nm	Integrated from 300 nm			
Oven-made (sample 1)	1.2%	0.94%	0.84%	0.67%	2.9	None
Flame made (sample 2)	9.08%	8.86%	7.62%	5.63%	2.65	1.6
Flame made on grooved Ti surface (sample 3)	11.31%	11.16%	8.41%	7.62%	2.65	1.6
Spray pyrolysis and Flame made (sample 4)	14.04%	13.79%	12.89%	12.26%	2.65	1.4

FIGURE 14: SEM images for a CM-n-TiO$_2$ (sample 2) [21–23].

FIGURE 15: X-ray diffraction (XRD) patterns for samples 1, 2 and 3, and identified as S1, S2, and S3, respectively [21–23].

in this wavelength region (see Figure 6). Furthermore, it should be noted that the carbon modification or doping was confined to surface region (2.0 nm deep) in CM-n-TiO$_2$, the absorption of light in the visible region was found low.

2.1.9. Scanning Electron Microscopy (SEM) of CM-n-TiO$_2$ Films. The surface characterization of a CM-n-TiO$_2$ film (sample 2) was performed by employing a scanning electron microscope (SEM) and the image is shown in Figure 14. The surface looks extremely rough and nanocrystalline nanowalls hence provided much higher surface area to absorb incident light, multiple absorption, and reflection to absorb more light and consequently generated enhanced photoresponse. Generation of multiple electron-hole pairs (excitons) by absorption of single high-energy photon in UV-region in nanocrystals (Ncs) was observed and also explained theoretically in terms of impact ionization [86–92]. Furthermore, the microscopic rough surface could temporarily trap microscopic oxygen gas bubbles on rough surface that may have acted as tiny lens and spherical mirrors that helped to concentrate the incident light [93] on the electrode surface and hence augmented the photoresponse for water splitting by an order of magnitude.
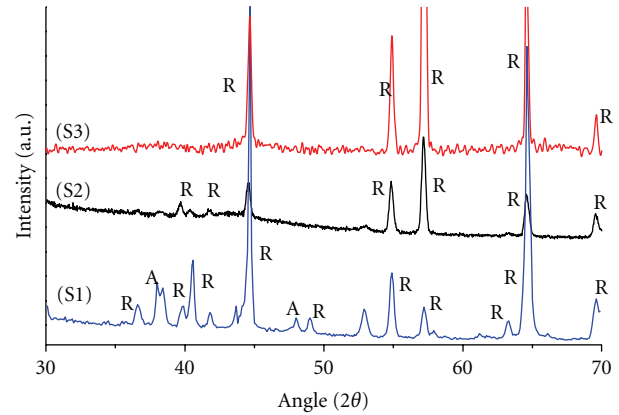
2.1.10. X-Ray Diffraction (XRD) for Titanium Oxides. X-ray diffraction (XRD) measurements were carried out to characterize the structure of n-TiO$_2$ and CM-n-TiO$_2$ samples. Figure 15 shows the XRD patterns for oven-made n-TiO$_2$ (S1); CM-n-TiO$_2$ synthesized by only thermal flame oxidation (S2) and the CM-n-TiO$_2$ synthesized by spray pyrolysis and thermal flame oxidation (S3).

The peaks of these XRD spectra of both CM-n-TiO$_2$ photoelectrodes (S2 and S3) are consistent with the rutile structure. The XRD results demonstrate that the crystal structure of oven-made n-TiO$_2$ (S1) is of mixture of anatase and rutile forms. It is important to note that some peaks of rutile structure are missing in both CM-n-TiO$_2$ samples (S2 and S3) compared to those in oven-made n-TiO$_2$ (S1). This indicates the marked influence of carbon modification on the structure of n-TiO$_2$.

2.1.11. Energy-Dispersive Spectroscopy (EDS) for CM-n-TiO$_2$ Films. Figure 16 shows the pattern of energy-dispersive spectroscopic (EDS) data for samples 1, 2, 3, and 4.
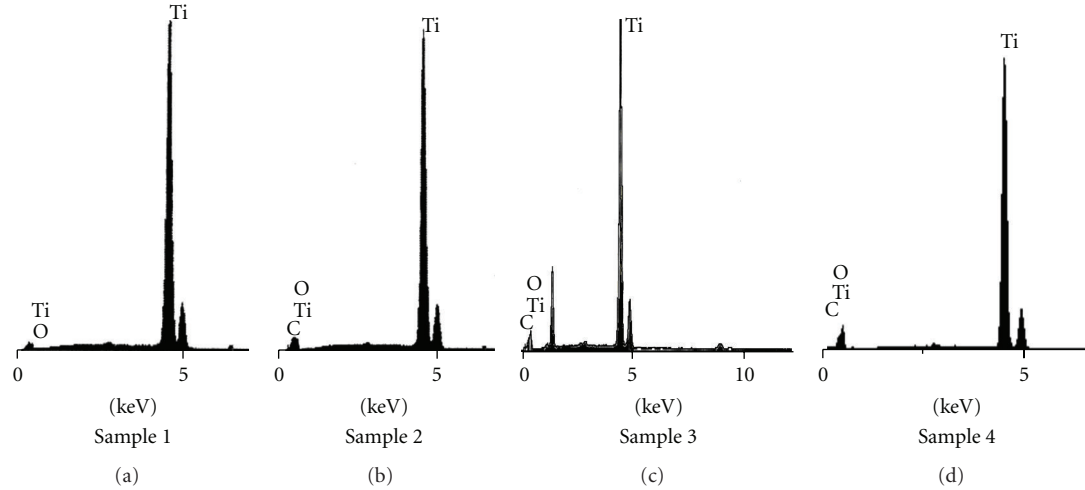
FIGURE 16: Pattern of energy-dispersive spectroscopy (EDS) of samples 1, 2, 3, and 4 [21–23].

The carbon contents increased significantly from 17.60 atom % for CM-n-TiO$_2$ synthesized by only thermal flame oxidation to 23.23 atom % for CM-n-TiO$_2$ synthesized by combination of spray pyrolysis and thermal flame oxidation (see Table 2 for detail).

2.2. Visible Light Active Hydrogen-Modified n-Type Titanium Oxide (HM-n-TiO$_2$) Thin Films.

Frites and Khan [94] reported a new method for the synthesis of hydrogen-modified (HM)-n-TiO$_2$ thin films by thermal oxidation of Ti metal sheet (Alfa Co. 0.25 mm thick) to TiO$_2$ in an electric oven followed by incorporation of hydrogen in it by electrochemical generation of hydrogen gas on it under cathodic polarization at −1.6 V versus Pt in an alkaline medium at room temperature and also provided its photo-electrochemical behavior during water-splitting reactions.

2.2.1. Photocurrent Density-Potential Dependence for HM-n-TiO$_2$.

The photoresponse of the HM-n- TiO$_2$ was evaluated by measuring the rate of water-splitting reaction to hydrogen and oxygen in terms of photocurrent density, J_p. The optimized electric oven-made n-TiO$_2$ and HM-n-TiO$_2$ photoelectrodes showed photocurrent densities of 0.2 mA cm^{-2} and 1.60 mA cm^{-2}, respectively, at a measured potential of −0.4 V versus Pt at illumination intensity of 100 mWcm^{-2} from a 150 W Xenon lamp (Figure 17). This indicated an *eightfold* increase in photocurrent density for HM-n-TiO$_2$ compared to oven-made n-TiO$_2$ at the same measured electrode potential. The band-gap energy of HM-n-TiO$_2$ was found to be 2.7 eV compared to 2.82 eV for electric oven-made n-TiO$_2$ and a mid-gap band at 1.67 eV above the valence band was also observed. The HM-n-TiO$_2$ thin-film photoelectrodes were characterized using photocurrent density under monochromatic light illumination and *UV-Vis* spectral measurements.

2.2.2. Monochromatic Photocurrent-Wavelength Dependence for HM-n-TiO$_2$.

The monochromatic photocurrent density, $J_p(\lambda)$, was measured under wavelength, λ, dependent

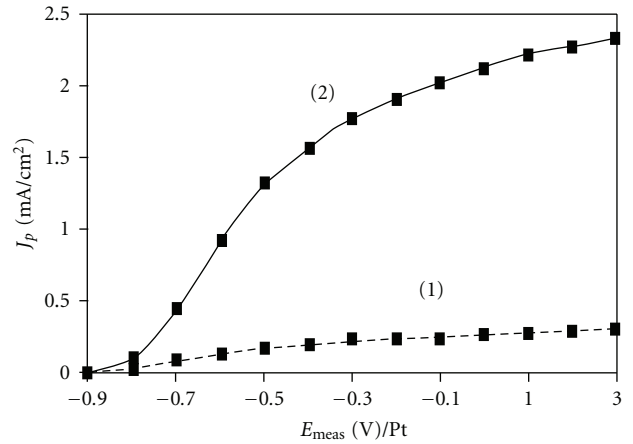FIGURE 17: Photocurrent density, J_p, as a function of measured potential, E_{meas} (V versus Pt) at light intensity of 100 mW/cm^2 from a 150 W Xenon lamp for (1) oven-made n-TiO$_2$ at 835°C for 5 min and (2) HM-n-TiO$_2$ samples [94].

monochromatic light illumination from a Xenon lamp by using a Spectra Physics monochromator (Model 77250) at a measured potential of −0.1 V versus Pt (see Figure 18). Performing integration under the curve in the wavelength range between 250 nm and 775 nm in Figure 18, a total photocurrent density of 2.2 mA/cm^2 was observed at HM-n-TiO$_2$ electrode. This value is little higher within the experimental error than the corresponding photocurrent density values of 2.1 mA/cm^2 for HM-n-TiO$_2$ samples under white light illumination, at the same measured potential of −0.1 V versus Pt (see Figure 17). The monochromatic photocurrent density versus wavelength plots shows a clear shift of the photosensitivity of the HM-n-TiO$_2$ to the visible region with a second peak around 630 nm compared to oven-made n-TiO$_2$ which shows only one pick in the UV region only (see Figure 18).

2.2.3. Bandgap Energy Determination for HM-n-TiO$_2$.

The bandgap of HM-n-TiO$_2$ becomes narrower from 3.0 eV for

TABLE 2: Atomic percent of elements Ti, O, and C in n-TiO$_2$ and CM-n-TiO$_2$ films from EDS data.

Element	Atomic %			
	Flat n-TiO$_2$ by flame	CM-n-TiO$_2$ by flame	Grooved CM-n-TiO$_2$ by flame	CM-n-TiO$_2$ by spray and flame
Ti	33.33	15.73	13.96	10.10
O	66.66	66.67	66.67	66.67
C	0	17.60	19.38	23.23
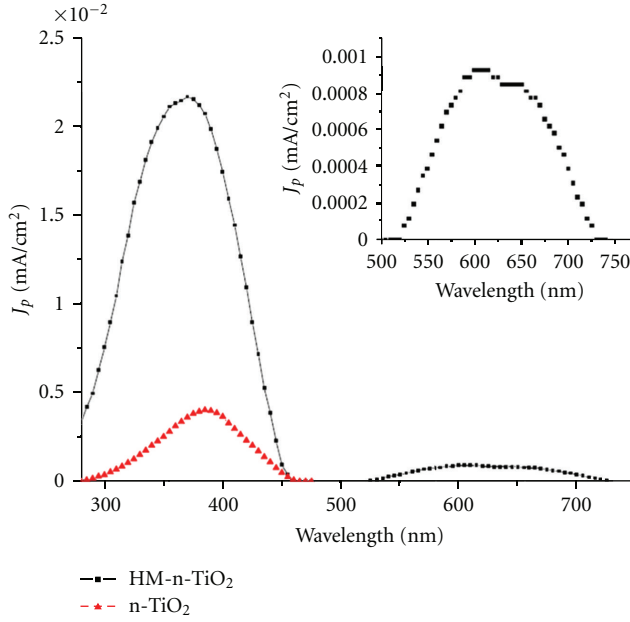
FIGURE 18: The monochromatic photocurrent density, $J_p(\lambda)$, as a function of wavelength of light, λ (nm), for HM-n-TiO$_2$, and unreduced n-TiO$_2$ under monochromatic light illumination from a Xenon lamp; using a Spectra Physics monochromator (Model 77250) with a 0.75 mm slit width. The applied potential was kept at −0.1 V/Pt for both electrodes [94].

regular rutile TiO$_2$ to 2.7 eV (Figure 19). Also, a mid-gap band was created within the bandgap of n-TiO$_2$ due to hydrogen reduction; which is located 1.67 eV above the valence band for the hydrogen-modified titanium oxide.

2.3. Carbon-Modified Iron Oxides (CM-n-Fe$_2$O$_3$) Thin Films.
Shaban and Khan [23] synthesized nanocrystalline carbon-modified iron (III) oxide (CM-n-Fe$_2$O$_3$) thin films by flame oxidation of Fe metal sheet at different temperatures (700–850°C) and oxidation time (3–15 min), using a custom-designed large area flame (Knight, model RN. 3.5 xa wc) under controlled oxygen and natural gas flows.

2.3.1. Photocurrent Density-Potential Dependence for Iron Oxides Photoelectrodes.
Figure 20 shows the dependence of photocurrent density (J_p, mA cm^{-2}) for water splitting on measured electrode potentials (E_{meas}, V/SCE) at light intensity of 100 mW cm^{-2}, for oven-made-n-Fe$_2$O$_3$ (sample A) and flame-made CM-n-Fe$_2$O$_3$ (sample B). Under illumination of light intensity of 100 mW cm^{-2}, and at measured
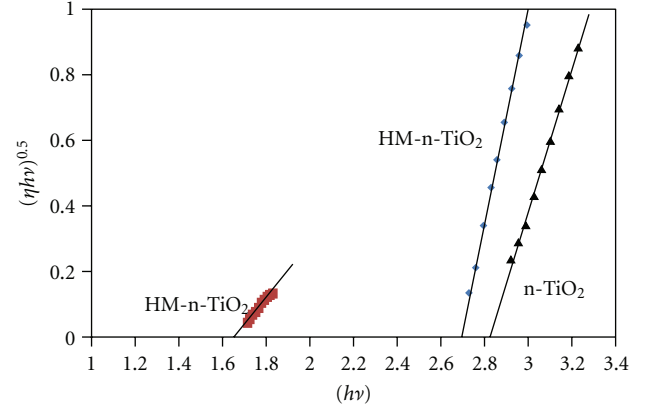

FIGURE 19: $[\eta(\lambda)h\nu]^{1/2}$ versus $h\nu$ plot for electric oven-made n-TiO$_2$ and hydrogen-modified HM-n-TiO$_2$ films [94].
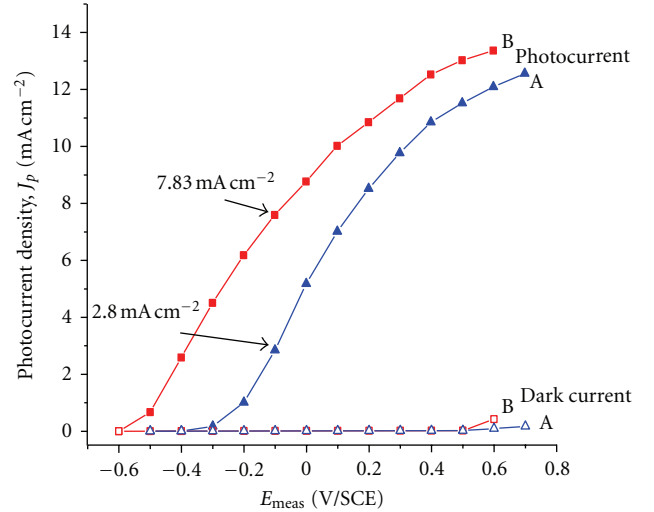

FIGURE 20: Photocurrent density (j_p, mAcm^{-2}) versus measured potential (E_{meas}, V/SCE) for oven-made n-Fe$_2$O$_3$ (sample A) and flame-made CM-n-Fe$_2$O$_3$ (sample B) under light intensity of 100 mW cm^{-2}. Both samples were prepared at the same optimum conditions of 850°C for 15 minutes. 5.0 M KOH was used as an electrolyte solution [23].

potential of −0.1 V/SCE, photocurrent density increased from 2.8 mA cm^{-2} for oven-made n-Fe$_2$O$_3$ to 7.83 mA cm^{-2} for carbon-modified n-CM-n-Fe$_2$O$_3$ synthesized by thermal flame oxidation. The electrode potentials at open circuit condition under illumination of light, E_{aoc}, were found to be −0.498 V/SCE and −0.510 V/SCE for samples A and B, respectively.
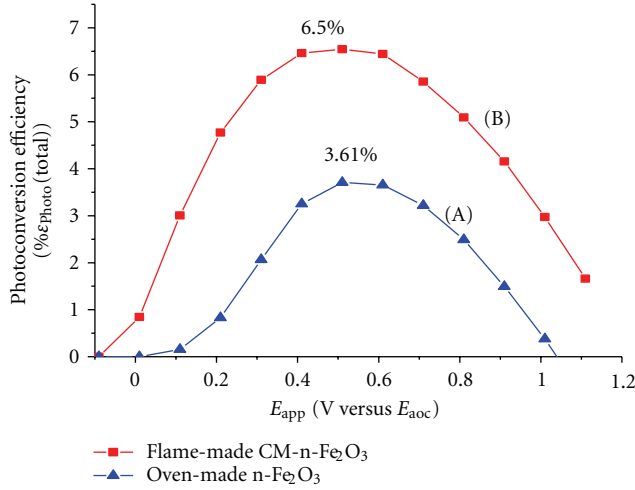
FIGURE 21: Photoconversion efficiency, $\%\varepsilon_{photo}(total)$, at light intensity of 100 mWcm^{-2} versus applied potential, E_{app} (V versus E_{meas}) for oven-made n-Fe$_2$O$_3$ (samples A) and flame-made CM-n-Fe$_2$O$_3$ (sample B) [23].

FIGURE 23: The photoconversion efficiency, $\%\varepsilon_{photo}(\lambda)$, as a function of wavelength of light, λ, for CM-Fe$_2$O$_3$ [23].

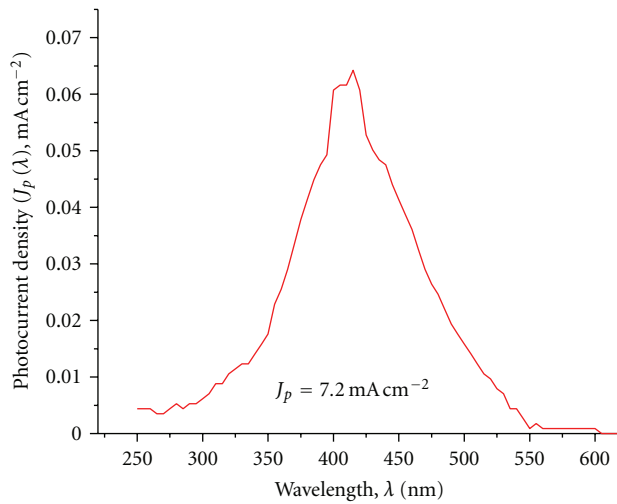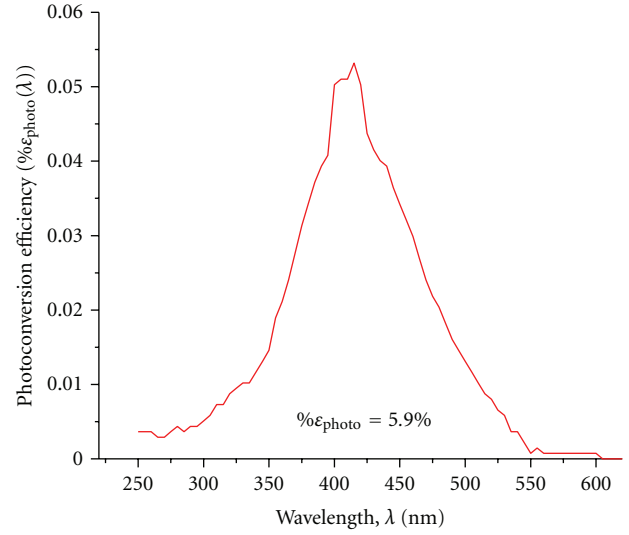

FIGURE 22: The monochromatic photocurrent density, $j_p(\lambda)$, as a function of wavelength of light, λ, for CM-Fe$_2$O$_3$ [23].
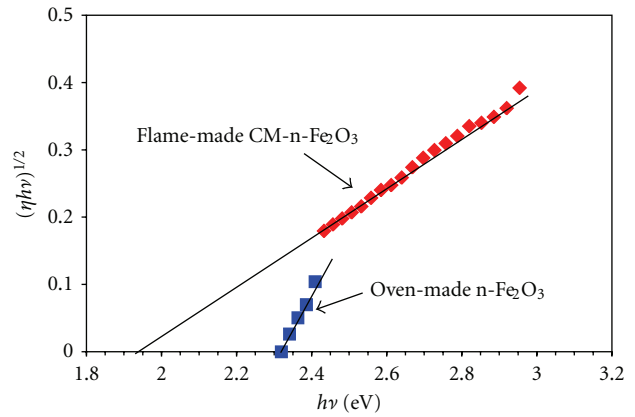

FIGURE 24: The respective plot of $[\eta(h\nu)]^{1/2}$ versus $h\nu$ to determine the bandgap energies of both oven-made n-Fe$_2$O$_3$ and flame-made CM-n-Fe$_2$O$_3$ films [23].

2.3.2. Photoconversion Efficiency-Potential Dependence for Iron Oxides Photoelectrodes.

Figure 21 shows the photoconversion efficiency, $\%\varepsilon_{photo}(total)$, as a function of applied potential, E_{app} (V versus E_{meas}), for samples A and B. Under illumination intensity of 100 m W cm^{-2}, the maximum photoconversion efficiency for water splitting improved significantly from 3.61% (at a minimal applied potential of +0.5 V versus E_{aoc}) for sample A 6.5% (at a minimal applied potential of +0.402 V versus E_{aoc}) for sample B.

2.3.3. Monochromatic Photocurrent-Wavelength Dependence for Iron Oxides.

The dependence of monochromatic photocurrent density, $j_p(\lambda)$, versus the wavelength, λ, of light for CM-n-Fe$_2$O$_3$ (sample B) is shown in Figure 22. The monochromatic photocurrent density, $j_p(\lambda)$, at measured potential of 0.0 V/SCE was measured under monochromatic light illumination from a 150 watt Xenon lamp by using a spectra physics monochromator (Model 77250). Performing integration under the curve, total photocurrent densities of 7.2 mA cm^{-2} were found for CM-n-Fe$_2$O$_3$. This value is less than that under white light illumination (7.83 mA cm^{-2}). This is due to loss of light through the monochromator. It is also due to steady-state measurements of photocurrents under monochromatic light illumination. Note that the photocurrent densities under white light illumination were measured with a scan rate of 50 mV/sec.

2.3.4. Photoconversion Efficiency from Monochromatic Photocurrent Densities at Iron Oxide Electrodes.

The plot of $\%\varepsilon_{photo}(\lambda)$ versus wavelength, λ, using (10) for CM-n-Fe$_2$O$_3$ is given in Figure 23 where total intensity in the denominator of (10) was used as 100 mW cm^{-2}. Performing integration
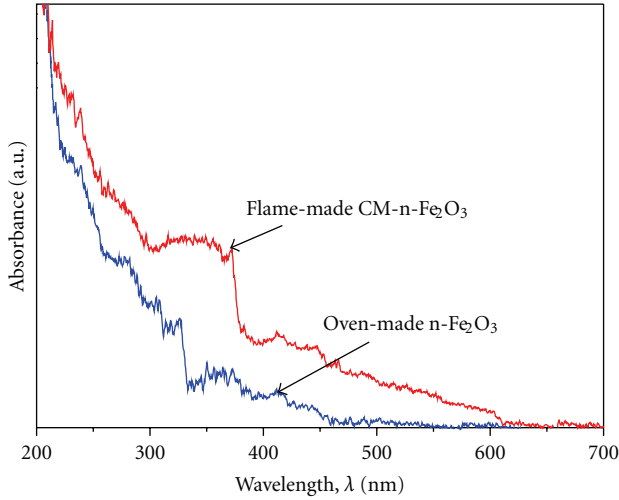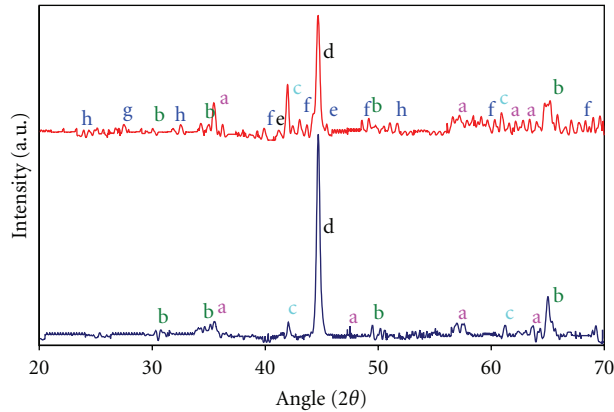
FIGURE 25: UV-visible spectra for iron oxides [23].

FIGURE 26: X-ray diffraction (XRD) patterns for flame-made CM-n-Fe$_2$O$_3$ (top plot) and the reference oven-made n-Fe$_2$O$_3$(bottom plot) films. The detected probable formulas to comply with peaks are a = Fe$_2$O$_3$; b = Fe$_3$O$_4$; c = FeO; d = Fe; e = FeC; f = Fe$_2$C; g = Fe$_3$C; h = FeCO$_3$ [23].

TABLE 3: Atomic percent of elements Fe, O, and C in n-Fe$_2$O$_3$ and CM-n- Fe$_2$O$_3$ films from EDS data.

Element	Atomic %	
	Oven-made n-Fe$_2$O$_3$	Flame-made CM-n-Fe$_2$O$_3$
Fe	43.7	36.2
O	56.3	55.4
C	0.0	8.4

in (8) from $\lambda_{\min}$ = 250 nm to λ_g = 1240/Eg or determining the area under the curve in **Figure 23** obtained using (10), a total photoconversion efficiency of 5.9% is also lower than that under white light illumination (6.5%) for the reasons mentioned in the above conditions.

2.3.5. Bandgap Energy Determination for Iron Oxides. **Figure 24** shows $[\eta(h\nu)]^{1/2}$ versus $h\nu$ for samples A and B, respectively. From the intercept of these plots, the bandgaps

were found to be 2.3 eV and 1.95 eV for samples A and B, respectively. These bandgap values are in agreement with those obtained from *UV-Vis* spectra (see **Figure 25**). Note that $\eta(\lambda)$ is the wavelength, λ, dependent quantum efficiency as expressed in (12).

2.3.6. UV-Vis Spectra for Iron Oxides. **Figure 25** compares the *UV-Vis* absorbance of flame-made CM-n-Fe$_2$O$_3$ and oven-made n-Fe$_2$O$_3$ photoelectrodes having maximum photoconversion efficiencies of 6.5% and 3.61%, respectively. Both electrodes were synthesized at the same optimum conditions of 850°C for 15 min. The *UV-Vis* spectroscopic results show a significant increase in the absorbance of light in the UV as well as in the visible regions for flame-made CM-n-Fe$_2$O$_3$ film compared to that of the oven-made n-Fe$_2$O$_3$. The *UV-Vis* spectra are consistent with the higher photocurrent densities of flame-made CM-n-Fe$_2$O$_3$ thin-film electrodes. The absorption spectra demonstrate a wide absorption in the UV and visible regions with a tail extending up to 600 nm which corresponds to a bandgap energy of 1.95 eV for flame-made CM-n-Fe$_2$O$_3$ and up to 545 nm which corresponds to bandgap energy of 2.3 eV for oven-made n-Fe$_2$O$_3$. The low bandgap energy value for flame-made CM-n-Fe$_2$O$_3$ can be attributed to carbon incorporation during the flame oxidation process of Fe metal sheet.

2.3.7. X-Ray Diffraction (XRD) for Iron Oxides. XRD patterns (**Figure 26**) show that in addition to Fe$_2$O$_3$, Fe$_3$O$_4$ and FeO are also present in both oven-made and flame-made thin films. Analysis of XRD confirms carbon incorporation in flame-made iron (III) oxide film (sample B) by the presence the peaks for iron carbide compounds in the forms of FeC, Fe$_2$C, Fe$_3$C, and FeCO$_3$. None of these peaks for iron carbide compounds were observed in oven-made iron (III) oxide (sample A). It can be concluded that the flame oxidation process is responsible for carbon incorporation onto iron (III) oxide thin film.

2.3.8. Energy-Dispersive Spectroscopy (EDS) for Iron Oxides. **Table 3** shows the EDS results of oven-made n-Fe$_2$O$_3$ (sample A) and flame-made CM-n-Fe$_2$O$_3$ (sample B) photoelectrodes. The presence of carbon in CM-n-Fe$_2$O$_3$ photoelectrode and its absence in the oven-made n-Fe$_2$O$_3$ were observed. The corresponding EDS spectra of oven-made n-Fe$_2$O$_3$ and flame-made CM-n-Fe$_2$O$_3$ samples are shown in Figures 27(a) and 27(b), respectively. Note that the regular oven-made n-Fe$_2$O$_3$ did not show any carbon peak.

2.3.9. Scanning Electron Microscopic (SEM) Images of Iron Oxides. Morphological differences were observed from the scanning electron microscopic (SEM) images (**Figure 28**) between (a) oven-made n-Fe$_2$O$_3$ film and (b) flame-made CM-n-Fe$_2$O$_3$ film. The surface of oven-made n-Fe$_2$O$_3$ shows nanowires but CM-n-Fe$_2$O$_3$ surface of sample B does not show nanowires even at higher magnification (200 nm compared to 1 micro meter used for oven-made sample a). The nanowires on oven-made n-Fe$_2$O$_3$ films (**Figure 28(a)**)
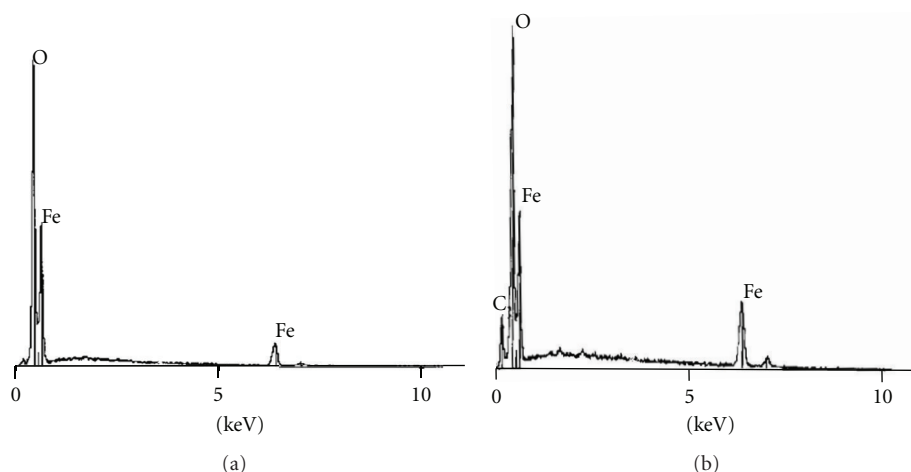
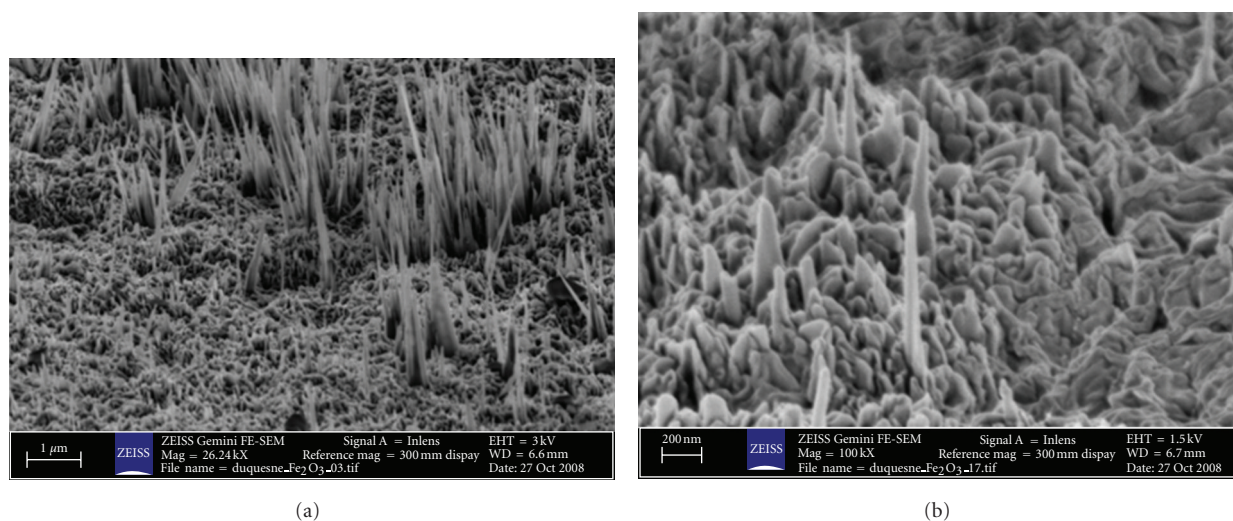Figure 27: Pattern of energy-dispersive spectroscopy (EDS) of samples (a) and (b) [23].

Figure 28: SEM images of (a) oven-made-n Fe_2O_3 [23] and (b) flame-made CM-n-Fe_2O_3 films.

helped to minimize the recombination rate of photogenerated carriers and consequently generated much higher photoresponse compared to its nanocrystalline thin films synthesized by spray pyrolysis methods earlier (4). The CM-n-Fe_2O_3 films show only the nanocrystals (Figure 28(b)).

2.4. Visible Light Active Carbon-Modified p-Type Tungsten Oxides (CM)-p-WO_3 Thin Film.
Shaban and Khan [84] synthesized carbon-modified p-type tungsten oxide (CM-p-WO_3) photoelectrodes by flame oxidation of tungsten metal sheets (Alfa Co. 0.25 mm thick) at several temperatures for different lengths of time.

2.4.1. Photocurrent Density-Potential Dependence for Tungsten Oxides Photoelectrodes.
The photocatalytic activity of CM-p-WO_3 was evaluated by measuring the rate of water-splitting reaction to hydrogen and oxygen, which is proportional to photocurrent density, j_p. Carbon-modified tungsten oxide photoelectrodes exhibited p-type photoresponse in acidic medium of 0.5 M H_2SO_4. The highest photocurrent density of 2.08 mA cm^{-2} was observed under illumination intensity of 80 mW cm^{-2} from a 150 Watt (Kratos Model LH 150/1) Xenon arc lamp at an optimal thermal oxidation temperature of 900°C for 15 min at applied potential of −0.4 V versus E_{aoc} (Figure 29).

2.4.2. Photoconversion Efficiency-Potential Dependence for Tungsten Oxides Photoelectrodes.
The optimized CM-p-WO_3 photoelectrodes were found to generate the highest photoconversion efficiency of 2.16% for photosplitting of water (Figure 30).

2.4.3. Monochromatic Photocurrent Density-Wavelength Dependence for CM-p-WO_3 Electrodes.
The dependence of monochromatic photocurrent density, $j_p(\lambda)$, versus the wavelength, λ, of light for CM-p-WO_3 thin-film electrodes, having photoconversion efficiency of 2.16% (synthesized by thermal oxidation of W metal at oxidation temperature of 900°C for 15 minutes), is shown in Figure 31.
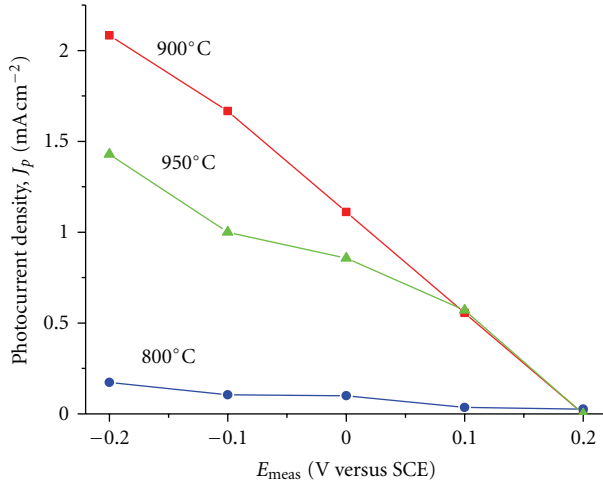
FIGURE 29: Photocurrent density (j_p, mAcm^{-2}) versus measured potential (E_{meas}, V/SCE) for CM-p-WO$_3$ synthesized by thermal oxidation of tungsten metal sheets at different flame temperatures 850, 900, and 950°C. All these samples were synthesized at the same flame oxidation time of 15 minutes [84].

FIGURE 30: Photoconversion efficiency (%ε_{photo}(total)) versus measured potential (E_{meas}, V/SCE) for CM-p-WO$_3$ synthesized by thermal oxidation of tungsten metal sheets at different flame temperatures 850, 900, and 950°C. All these samples were synthesized at the same flame oxidation time of 15 minutes [84].
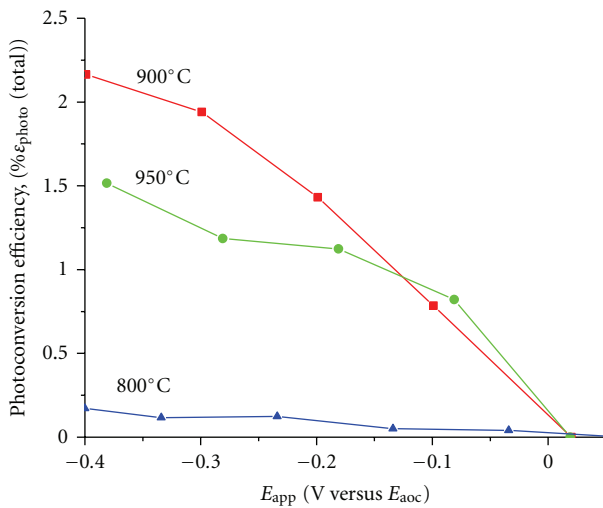
Significant visible light absorption activity by carbon-modified p-WO$_3$ can be noticed, where a maximum monochromatic photocurrent density value of 3.25 μA cm^{-2} at 425 nm was observed.

2.4.4. Dependence of Percent Incident Photon Conversion Efficiency (IPCE %) on Wavelength of Light, λ. Maximum IPCE (%) of 42.7% at wavelength of 260 nm can be observed (Figure 32). However, in the visible region, the CM-p-WO$_3$ shows incident photon conversion efficiency percent (IPCE %) in the range between 0.9% at 500 nm and 9.9% at 400 nm. These activities in the visible region can be attributed to
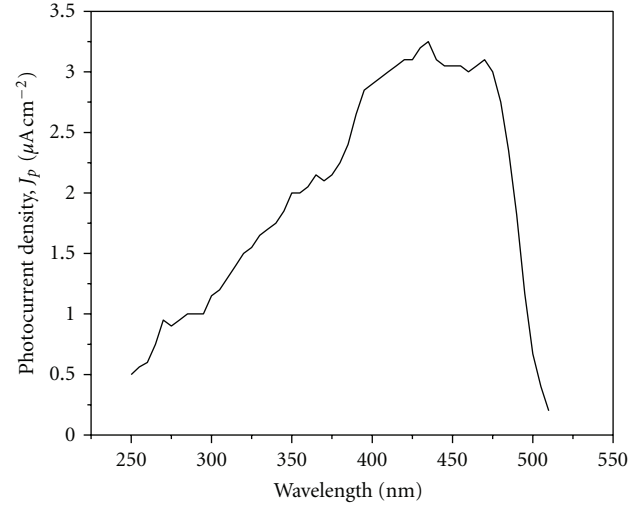

FIGURE 31: Monochromatic photocurrent density, $j_p(\lambda)$, versus the wavelength, λ, of light for CM-p-WO$_3$ thin-film electrodes synthesized by thermal oxidation of W metal at temperature of 900°C for 15 minutes; electrolyte solution of 0.5 M H$_2$SO$_4$; under monochromatic light illumination of Xenon lamp; using a Spectra Physics monochrometer (Model 77250) with a 0.75 mm slit width, and Silicon detector (UDT Sensors. Inc. Model 10DP/SB) [84].
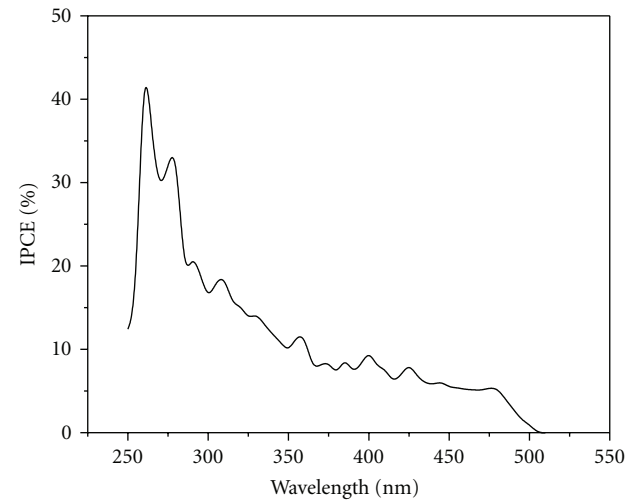
FIGURE 32: Incident photon conversion efficiency percent (IPEC %) as a function of wavelength, λ, of light for CM-p-WO$_3$ synthesized by thermal oxidation of W metal at temperature of 900°C for 15 minutes; electrolyte solution of 0.5 M H$_2$SO$_4$; under monochromatic light illumination of Xenon lamp; using a Spectra Physics monochrometer (Model 77250) with a 0.75 mm slit width, and Silicon detector (UDT Sensors. Inc. Model 10DP/SB) [84].

carbon modification of WO$_3$ during the flame oxidation process of tungsten metal.

2.4.5. Bandgap Energy. Figure 33 shows the plot for $[\eta(h\nu)]^{1/2}$ versus $h\nu$ for thermally prepared CM-p-WO$_3$ at oxidation temperature of 900°C for 15 min. From the intercept of the straight line, the bandgap is obtained. It can be

FIGURE 33: Plot of $[\eta(h\nu)]^{1/2}$ versus $h\nu$ to determine the bandgap of CM-p-WO$_3$ thin-film electrodes synthesized by thermal oxidation of W metal at temperature of 900°C for 15 minutes; electrolyte solution of 0.5 M H$_2$SO$_4$; under monochromatic light illumination of Xenon lamp; using a Spectra Physics monochromoter (Model 77250) with a 0.75 mm slit width, and Silicon detector (UDT Sensors. Inc., Model 10DP/SB) [84].
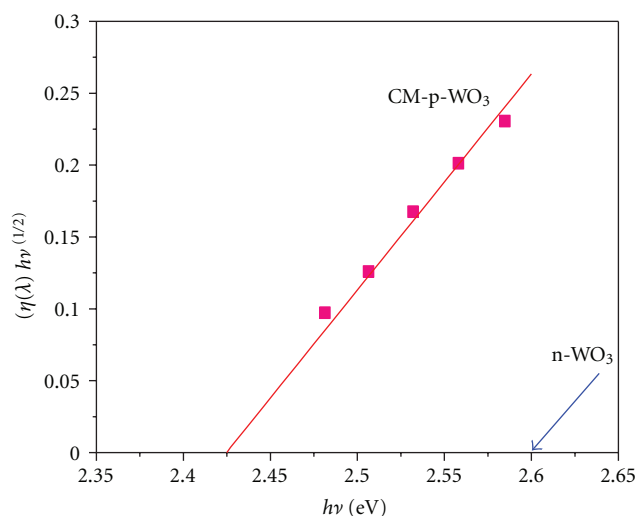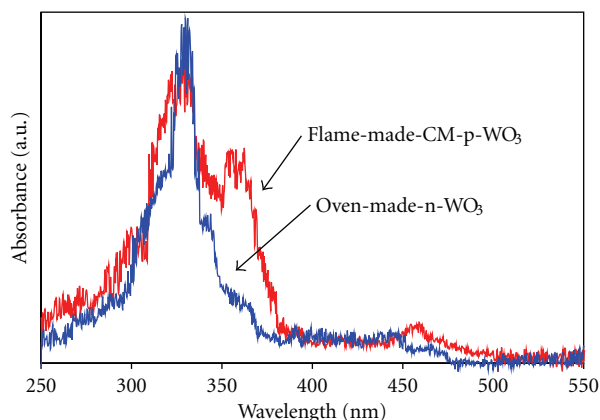

FIGURE 34: UV-Visible spectra of flame-made-CM-p-WO$_3$ and oven-made n-WO$_3$ photoelectrodes synthesized by heating at temperature of 900°C for 15 minutes [84].

observed that the bandgap energy became lower from 2.6 eV for regular n-WO$_3$ (to 2.42 eV for of CM-p-WO$_3$). This low bandgap energy can be attributed to carbon incorporation during the flame oxidation process of tungsten metal.

2.4.6. UV-Vis Spectra on CM-p-WO$_3$. The *UV-Vis* absorption spectra show (Figure 34) a significant improvement in the absorbance of light in UV and visible regions for flame-made CM-p-WO$_3$ films compared to oven-made n-WO$_3$. The absorption spectra of flame-made p-WO$_3$ show higher absorption in the visible region with a tail extending to 512 nm which corresponds to bandgap energy value of 2.42 eV.

The threshold of absorption for oven-made-n-WO$_3$ is at 475 nm (2.6 eV) which is in agreement with a bandgap value of 2.6 eV for n-WO$_3$ [74, 75]. The low bandgap energy value of 2.42 eV for CM-p-WO$_3$ films can be attributed to the carbon incorporation during the flame oxidation process of tungsten metal sheet. This low bandgap energy values for CM-p-WO$_3$ determined by *UV-Vis* spectra (Figure 34) agree well with the values obtained from the monochromatic photocurrent densities and the corresponding quantum efficiencies (Figure 33).

References

[1] S. U. M. Khan, M. Al-Shahry, and W. B. Ingler Jr., "Efficient photochemical water splitting by a chemically modified n-TiO$_2$," *Science*, vol. 297, no. 5590, pp. 2243–2245, 2002.

[2] S. Licht, B. Wang, S. Mukerji, T. Soga, M. Umeno, and H. Tributsch, "Efficient solar water splitting, exemplified by RuO$_2$-catalyzed AlGaAs/Si photoelectrolysis," *Journal of Physical Chemistry B*, vol. 104, no. 38, pp. 8920–8924, 2000.

[3] O. Khaselev and J. A. Turner, "A monolithic photovoltaic-photoelectrochemical device for hydrogen production via water splitting," *Science*, vol. 280, no. 5362, pp. 425–427, 1998.

[4] S. U. M. Khan and J. Akikusa, "Photoelectrochemical splitting of water at nanocrystalline n-Fe$_2$O$_3$ thin-film electrodes," *Journal of Physical Chemistry B*, vol. 103, no. 34, pp. 7184–7189, 1999.

[5] S. U. M. Khan and J. Akikusa, "Stability and photoresponse of nanocrystalline n-TiO$_2$ and n-TiO$_2$/Mn$_2$O$_3$ thin film electrodes during water splitting reactions," *Journal of the Electrochemical Society*, vol. 145, no. 1, pp. 89–93, 1998.

[6] J. Akikusa and S. U. M. Khan, "Photoresponse and AC impedance characterization of n-TiO$_2$ films during hydrogen and oxygen evolution reactions in an electrochemical cell," *International Journal of Hydrogen Energy*, vol. 22, no. 9, pp. 875–882, 1997.

[7] S. A. Majumder and S. U. M. Khan, "Photoelectrolysis of water at bare and electrocatalyst covered thin film iron oxide electrode," *International Journal of Hydrogen Energy*, vol. 19, no. 11, pp. 881–887, 1994.

[8] O. N. Srivastava, R. K. Karn, and M. Misra, "Semiconductor-septum photoelectrochemical solar cell for hydrogen production," *International Journal of Hydrogen Energy*, vol. 25, no. 6, pp. 495–503, 2000.

[9] T. Bak, J. Nowotny, M. Rekas, and C. C. Sorrell, "Photoelectrochemical properties of the TiO$_2$-Pt system in aqueous solutions," *International Journal of Hydrogen Energy*, vol. 27, no. 1, pp. 19–26, 2002.

[10] J. Akikusa and S. U. M. Khan, "Photoelectrolysis of water to hydrogen in p-SiC/Pt and p-SiC/n-TiO$_2$ cells," *International Journal of Hydrogen Energy*, vol. 27, no. 9, pp. 863–870, 2002.

[11] J. G. Yu, H. G. Yu, B. Cheng, X. J. Zhao, J. C. Yu, and W. K. Ho, "The effect of calcination temperature on the surface microstructure and photocatalytic activity of TiO$_2$ thin films prepared by liquid phase deposition," *Journal of Physical Chemistry B*, vol. 107, no. 50, pp. 13871–13879, 2003.

[12] N. Serpone and E. Pelizzetti, *Photocatalysis: Fundamentals and Applications*, Wiley, New York, NY, USA, 1989.

[13] J. Nowotny, T. Bak, M. K. Nowotny, and L. R. Sheppard, "Titanium dioxide for solar-hydrogen I. Functional properties," *International Journal of Hydrogen Energy*, vol. 32, no. 14, pp. 2609–2629, 2007.

[14] S. K. Mohapatra, V. K. Mahajan, and M. Misra, "Double-side illuminated titania nanotubes for high volume hydrogen generation by water splitting," *Nanotechnology*, vol. 18, no. 44, Article ID 445705, 2007.

[15] C. F. Chi, Y. L. Lee, and H. S. Weng, "A CdS-modified TiO_2 nanocrystalline photoanode for efficient hydrogen generation by visible light," *Nanotechnology*, vol. 19, no. 12, Article ID 125704, 2008.

[16] C. Xu and S. U. M. Khan, "Photoresponse of visible light active carbon-modified -n-Ti O_2 thin films," *Electrochemical and Solid-State Letters*, vol. 10, no. 3, pp. B56–B59, 2007.

[17] C. Xu, R. Killmeyer, M. L. Gray, and S. U. M. Khan, "Enhanced carbon doping of n-TiO_2 thin films for photoelectrochemical water splitting," *Electrochemistry Communications*, vol. 8, no. 10, pp. 1650–1654, 2006.

[18] S. K. Mohaputra, M. Mishra, and V. K. Mahajan, "Design of a highly efficient photoelectrolytic cell for hydrogen generation by water splitting: application of $TiO_{2-x}C_x$ nanotubes as a photoanode and Pt/TiO2 nanotubes as a cathode," *The Journal of Physical Chemistry C*, vol. 111, pp. 8677–8685, 2007.

[19] K. Noworyta and J. Augustynski, "Spectral photoresponses of carbon-doped TiO_2 film electrodes," *Electrochemical and Solid-State Letters*, vol. 7, no. 6, pp. E31–E33, 2004.

[20] Y. A. Shaban and S. U. M. Khan, "Visible light active carbon modified n-TiO_2 for efficient hydrogen production by photoelectrochemical splitting of water," *International Journal of Hydrogen Energy*, vol. 33, no. 4, pp. 1118–1126, 2008.

[21] Y. A. Shaban and S. U. M. Khan, "Surface grooved visible light active carbon modified (CM)-n-TiO_2 thin films for efficient photoelectrochemical splitting of water," *Chemical Physics*, vol. 339, no. 1–3, pp. 73–85, 2007.

[22] Y. A. Shaban and S. U. M. Khan, "Carbon modified (CM)-n-TiO_2 thin films for efficient water splitting to H_2 and O_2 under xenon lamp light and natural sunlight illuminations," *Journal of Solid State Electrochemistry*, vol. 13, no. 7, pp. 1025–1036, 2009.

[23] Y. A. Shaban and S. U. M. Khan, "Efficient photoelectrochemical splitting of water to H_2 and O_2 at nanocrystalline carbon modified (CM)-n-TiO_2 and (CM)-n-Fe_2O_3 thin films," *International Journal of Nanotechnology*, vol. 7, no. 1, pp. 69–98, 2010.

[24] Y. Li, D. S. Hwang, N. H. Lee, and S. J. Kim, "Synthesis and characterization of carbon-doped titania as an artificial solar light sensitive photocatalyst," *Chemical Physics Letters*, vol. 404, no. 1–3, pp. 25–29, 2005.

[25] H. Wang, T. Deutsch, and J. A. Turner, "Direct water splitting under visible light with nanostructured hematite and WO_3 photoanodes and a $GaInP_2$ photocathode," *Journal of the Electrochemical Society*, vol. 155, no. 5, pp. F91–F96, 2008.

[26] C. Sanchez, K. D. Sieber, and G. A. Somorjai, "The photoelectrochemistry of niobium doped α-Fe_2O_3," *Journal of Electroanalytical Chemistry*, vol. 252, no. 2, pp. 269–290, 1988.

[27] R. Shinar and J. H. Kennedy, "Photoactivity of doped αFe_2O_3 electrodes," *Solar Energy Materials*, vol. 6, no. 3, pp. 323–335, 1982.

[28] W. B. Ingler Jr., J. P. Baltrus, and S. U. M. Khan, "Photoresponse of p-Type zinc-doped iron(III) oxide thin films," *Journal of the American Chemical Society*, vol. 126, no. 33, pp. 10238–10239, 2004.

[29] W. B. Ingler Jr. and S. U. M. Khan, "Photoresponse of spray pyrolytically synthesized copper-doped p-Fe_2O_3 thin film electrodes in water splitting," *International Journal of Hydrogen Energy*, vol. 30, no. 8, pp. 821–827, 2005.

[30] W. B. Ingler Jr. and S. U. M. Khan, "Photoresponse of spray pyrolytically synthesized magnesium-doped iron (III) oxide (p-Fe_2O_3) thin films under solar simulated light illumination," *Thin Solid Films*, vol. 461, no. 2, pp. 301–308, 2004.

[31] S. Virtanen, P. Schmuki, H. Böhni, P. Vuoristo, and T. Mäntylä, "Artificial Cr- and Fe-oxide passive layers prepared by sputter deposition," *Journal of the Electrochemical Society*, vol. 142, no. 9, pp. 3067–3072, 1995.

[32] P. Schmuki, M. Büchler, S. Virtanen, H. Böhni, R. Muller, and L. J. Gauckler, "Bulk metal oxides as a model for the electronic properties of passive films," *Journal of the Electrochemical Society*, vol. 142, no. 10, pp. 3336–3342, 1995.

[33] K. G. McGregor, M. Calvin, and J. W. Otvos, "Photoeffects in Fe_2O_3 sintered semiconductors," *Journal of Applied Physics*, vol. 50, no. 1, pp. 369–373, 1979.

[34] M. M. Khader, N. N. Lichtin, G. H. Vurens, M. Salmeron, and G. A. Somorjai, "Photoassisted catalytic dissociation of water and reduction of nitrogen to ammonia on partially reduced ferric oxide," *Langmuir*, vol. 3, pp. 303–304, 1987.

[35] A. Duret and M. Grätzel, "Visible light-induced water oxidation on mesoscopic α-Fe_2O_3 films made by ultrasonic spray pyrolysis," *Journal of Physical Chemistry B*, vol. 109, no. 36, pp. 17184–17191, 2005.

[36] I. Cesar, A. Kay, J. A. G. Martinez, and M. Grätzel, "Translucent thin film Fe_2O_3 photoanodes for efficient water splitting by sunlight: nanostructure-directing effect of Si-doping," *Journal of the American Chemical Society*, vol. 128, no. 14, pp. 4582–4583, 2006.

[37] M. Ni, M. K. H. Leung, D. Y. C. Leung, and K. Sumathy, "A review and recent developments in photocatalytic water-splitting using TiO_2 for hydrogen production," *Renewable and Sustainable Energy Reviews*, vol. 11, no. 3, pp. 401–425, 2007.

[38] J. Zhu and M. Zäch, "Nanostructured materials for photocatalytic hydrogen production," *Current Opinion in Colloid & Interface Science*, vol. 14, no. 4, pp. 260–269, 2009.

[39] A. L. Linsebigler, G. Lu, and J. T. Yates, "Photocatalysis on TiO_2 surfaces: principles, mechanisms, and selected results," *Chemical Reviews*, vol. 95, no. 3, pp. 735–758, 1995.

[40] A. Hagfeldt and M. Gratzel, "Light-induced redox reactions in nanocrystalline systems," *Chemical Reviews*, vol. 95, p. 49, 1995.

[41] A. Kudo, H. Kato, and I. Tsuji, "Strategies for the development of visible-light-driven photocatalysts for water splitting," *Chemistry Letters*, vol. 33, no. 12, pp. 1534–1539, 2004.

[42] W. Choi, A. Termin, and M. R. Hoffmann, "The role of metal ion dopants in quantum-sized TiO_2: correlation between photoreactivity and charge carrier recombination dynamics," *Journal of Physical Chemistry*, vol. 98, no. 51, pp. 13669–13679, 1994.

[43] M. Anpo, "Photocatalysis on titanium oxide catalysts—approaches in achieving highly efficient reactions and realizing the use of visible light," *Catalysis Surveys from Japan*, vol. 1, no. 2, pp. 169–179, 1997.

[44] S. Sakthivel and H. Kisch, "Daylight photocatalysis by carbon-modified titanium dioxide," *Angewandte Chemie—International Edition*, vol. 42, no. 40, pp. 4908–4911, 2003.

[45] Y. Choi, T. Umebayashi, and M. Yoshikawa, "Fabrication and characterization of C-doped anatase TiO_2 photocatalysts," *Journal of Materials Science*, vol. 39, no. 5, pp. 1837–1839, 2004.

[46] E. Barborini, A. M. Conti, I. Kholmanov et al., "Nanostructured TiO_2 films with 2 eV optical gaps," *Advanced Materials*, vol. 17, no. 15, pp. 1842–1846, 2005.

[47] D. Noguchi, Y. Kawamata, and T. Nagatomo, "The response of TiO$_2$ photocatalysts codoped with nitrogen and carbon to visible light," *Journal of the Electrochemical Society*, vol. 152, no. 9, pp. D124–D129, 2005.

[48] C. Xu, R. Killmeyer, M. L. Gray, and S. U. M. Khan, "Photocatalytic effect of carbon-modified n-TiO$_2$ nanoparticles under visible light illumination," *Applied Catalysis B*, vol. 64, no. 3-4, pp. 312–317, 2006.

[49] H. Irie, Y. Watanabe, and K. Hashimoto, "Carbon-doped anatase TiO$_2$ powders as a visible-light sensitive photocatalyst," *Chemistry Letters*, vol. 32, no. 8, pp. 772–773, 2003.

[50] R. Asahi, T. Morikawa, T. Ohwaki, K. Aoki, and Y. Taga, "Visible-light photocatalysis in nitrogen-doped titanium oxides," *Science*, vol. 293, no. 5528, pp. 269–271, 2001.

[51] Y. C. Hong, C. U. Bang, D. H. Shin, and H. S. Uhm, "Band gap narrowing of TiO$_2$ by nitrogen doping in atmospheric microwave plasma," *Chemical Physics Letters*, vol. 413, no. 4-6, pp. 454–457, 2005.

[52] T. Umebayashi, T. Yamaki, H. Itoh, and K. Asai, "Band gap narrowing of titanium dioxide by sulfur doping," *Applied Physics Letters*, vol. 81, no. 3, pp. 454–456, 2002.

[53] J. Tang, Y. Wu, E. W. McFarland, and G. D. Stucky, "Synthesis and photocatalytic properties of highly crystalline and ordered mesoporous TiO$_2$ thin films," *Chemical Communications*, vol. 10, no. 14, pp. 1670–1671, 2004.

[54] H. Choi, E. Stathatos, and D. D. Dionysiou, "Sol-gel preparation of mesoporous photocatalytic TiO$_2$ films and TiO$_2$/Al$_2$O$_3$ composite membranes for environmental applications," *Applied Catalysis B*, vol. 63, no. 1-2, pp. 60–67, 2006.

[55] G. K. Mor, K. Shankar, M. Paulose, O. K. Varghese, and C. A. Grimes, "Enhanced photocleavage of water using titania nanotube arrays," *Nano Letters*, vol. 5, no. 1, pp. 191–195, 2005.

[56] J. H. Park, S. Kim, and A. J. Bard, "Novel carbon-doped TiO$_2$ nanotube arrays with high aspect ratios for efficient solar water splitting," *Nano Letters*, vol. 6, no. 1, pp. 24–28, 2006.

[57] K. Shankar, M. Paulose, G. K. Mor, O. K. Varghese, and C. A. Grimes, "A study on the spectral photoresponse and photoelectrochemical properties of flame-annealed titania nanotube-arrays," *Journal of Physics D*, vol. 38, no. 18, pp. 3543–3549, 2005.

[58] C. Xu, Y. A. Shaban, W. B. Ingler Jr., and S. U. M. Khan, "Visible light active carbon modified (CM)-n-TiO$_2$ nanotubes for efficient photoelectrochemical splitting of water," *ECS Transactions*, vol. 3, pp. 65–73, 2006.

[59] C. Xu, Y. A. Shaban, W. B. Ingler Jr., and S. U. M. Khan, "Nanotube enhanced photoresponse of carbon modified (CM)-n-TiO$_2$ for efficient water splitting," *Solar Energy Materials and Solar Cells*, vol. 91, no. 10, pp. 938–943, 2007.

[60] R. Hahn, A. Ghicov, J. Salonen, V. P. Lehto, and P. Schmuki, "Carbon doping of self-organized TiO$_2$ nanotube layers by thermal acetylene treatment," *Nanotechnology*, vol. 18, no. 10, Article ID 105604, 2007.

[61] Y. Nakano, T. Morikawa, T. Ohwaki, and Y. Taga, "Electrical characterization of band gap states in C-doped TiO$_2$ films," *Applied Physics Letters*, vol. 87, no. 5, Article ID 052111, 2005.

[62] W. Ren, Z. Ai, F. Jia, L. Zhang, X. Fan, and Z. Zou, "Low temperature preparation and visible light photocatalytic activity of mesoporous carbon-doped crystalline TiO$_2$," *Applied Catalysis B*, vol. 69, no. 3-4, pp. 138–144, 2007.

[63] Y. Sun, C. J. Murphy, K. R. Reyes-Gil, E. A. Reyes-Garcia, J. P. Lilly, and D. Raftery, "Carbon-doped In$_2$O$_3$ films for photoelectrochemical hydrogen production," *International Journal of Hydrogen Energy*, vol. 33, no. 21, pp. 5967–5974, 2008.

[64] E. Cardenas, A. Arato, E. Perez-Tijerina, T. K. Das Roy, G. Alan Castllo, and B. Krishnan, "Carbon-doped Sb$_2$S$_3$ thin films: structural, optical and electrical properties," *Solar Energy Materials & Solar Cells*, vol. 93, pp. 33–36, 2009.

[65] X. Nie and K. Sohlberg, "The influence of surface reconstruction and c-impurities on photocatalytic water dissociation by TiO$_2$," in *Proceedings of the Materials Research Society Symposium on Materials and Technology for Hydrogen Economy*, G.-A. Nazri et al., Ed., vol. 801, p. 205, Boston, Mass, USA, December 2003.

[66] H. Wang and J. P. Lewis, "Effects of dopant states on photoactivity in carbon-doped TiO$_2$," *Journal of Physics Condensed Matter*, vol. 17, no. 21, pp. L209–L213, 2005.

[67] H. Wang and J. P. Lewis, "Second-generation photocatalytic materials: anion-doped TiO$_2$," *Journal of Physics Condensed Matter*, vol. 18, no. 2, pp. 421–434, 2006.

[68] C. Di Valentin, G. Pacchioni, and A. Selloni, "Theory of carbon doping of titanium dioxide," *Chemistry of Materials*, vol. 17, no. 26, pp. 6656–6665, 2005.

[69] S. Chandra, *Photoelectrochemical Solar Cells*, Gordon and Breach, New York, NY, USA, 1985.

[70] R. J. Komp, *Practical Photovoltaics: 'Electricity from Solar Cells'*, Aatec, Ann Arbor, Mich, USA, 3rd edition, 1995.

[71] S. H. Baeck, K. S. Choi, T. F. Jaramillo, G. D. Stucky, and E. W. McFarland, "Enhancement of photocatalytic and electrochromic properties of electrochemically fabricated mesoporous WO$_3$ thin films," *Advanced Materials*, vol. 15, no. 15, pp. 1269–1273, 2003.

[72] J. L. Solis, S. Saukko, L. Kish, C. G. Granqvist, and V. Lantto, "Semiconductor gas sensors based on nanostructured tungsten oxide," *Thin Solid Films*, vol. 391, no. 2, pp. 255–260, 2001.

[73] Y. Li, Y. Bando, and D. Golberg, "Quasi-aligned single-crystalline W$_{18}$O$_{49}$ nanotubes and nanowires," *Advanced Materials*, vol. 15, no. 15, pp. 1294–1296, 2003.

[74] C. Santato, M. Odziemkowski, M. Ulmann, and J. Augustynski, "Crystallographically oriented mesoporous WO$_3$ films: synthesis, characterization, and applications," *Journal of the American Chemical Society*, vol. 123, no. 43, pp. 10639–10649, 2001.

[75] J. L. Desplat, "Near-uv photon efficiency in a TiO$_2$ electrode: application to hydrogen production from solar energy," *Journal of Applied Physics*, vol. 47, no. 11, pp. 5102–5104, 1976.

[76] A. Rampaul, I. P. Parkin, S. A. O'Neill, J. DeSouza, A. Mills, and N. Elliott, "Titania and tungsten doped titania thin films on glass; active photocatalysts," *Polyhedron*, vol. 22, no. 1, pp. 35–44, 2003.

[77] N. S. Gaikwad, G. Waldner, A. Brüger, A. Belaidi, S. M. Chaqour, and M. Neumann-Spallart, "Photoelectrochemical characterization of semitransparent WO$_3$ films," *Journal of the Electrochemical Society*, vol. 152, no. 5, pp. G411–G416, 2005.

[78] M. A. Butler, R. D. Nasby, and R. K. Quinn, "Tungsten trioxide as an electrode for photoelectrolysis of water," *Solid State Communications*, vol. 19, no. 10, pp. 1011–1014, 1976.

[79] M. Spichiger-Ulmann and J. Augustynski, "Aging effects in n-type semiconducting WO$_3$ films," *Journal of Applied Physics*, vol. 54, no. 10, pp. 6061–6064, 1983.

[80] O. Bohnke, C. Bohnke, G. Robert, and B. Carquille, "Electrochromism in WO$_3$ thin films. I. LiClO4-propylene carbonate-water electrolytes," *Solid State Ionics*, vol. 6, no. 2, pp. 121–128, 1982.

[81] R. A. Batchelor, M. S. Burdis, and J. R. Siddle, "Electrochromism in sputtered WO$_3$ thin films," *Journal of the Electrochemical Society*, vol. 143, no. 3, pp. 1050–1055, 1996.

[82] N. Özer, "Optical and electrochemical characteristics of sol-gel deposited tungsten oxide films: a comparison," *Thin Solid Films*, vol. 304, no. 1-2, pp. 310–314, 1997.

[83] J. P. Cronin, D. J. Tarico, J. C. L. Tonazzi, A. Agrawal, and S. R. Kennedy, "Microstructure and properties of sol-gel deposited WO_3 coatings for large area electrochromic windows," *Solar Energy Materials and Solar Cells*, vol. 29, no. 4, pp. 371–386, 1993.

[84] Y. A. Shaban and S. U. M. Khan, "Visible Light Active Carbon Modified (CM)-p-WO3 Thin Film Electrodes for Photosplitting of Water,," *ECS Transactions*, vol. 6, no. 2, pp. 93–100, 2007.

[85] http://www.nrel.gov/.

[86] R. D. Schaller and V. I. Klimov, "High efficiency carrier multiplication in PbSe nanocrystals: Implications for solar energy conversion," *Physical Review Letters*, vol. 92, no. 18, pp. 186601–186605, 2004.

[87] R. J. Ellingson, M. C. Beard, J. C. Johnson et al., "Highly efficient multiple exciton generation in colloidal PbSe and PbS quantum dots," *Nano Letters*, vol. 5, no. 5, pp. 865–871, 2005.

[88] R. D. Schaller, M. Sykora, J. M. Pietryga, and V. I. Klimov, "Seven excitons at a cost of one: redefining the limits for conversion efficiency of photons into charge carriers," *Nano Letters*, vol. 6, no. 3, pp. 424–429, 2006.

[89] J. E. Murphy, M. C. Beard, A. G. Norman et al., "PbTe colloidal nanocrystals: synthesis, characterization, and multiple exciton generation," *Journal of the American Chemical Society*, vol. 128, no. 10, pp. 3241–3247, 2006.

[90] A. Shabaev, A. L. Efros, and A. J. Nozik, "Multiexciton generation by a single photon in nanocrystals," *Nano Letters*, vol. 6, no. 12, pp. 2856–2863, 2006.

[91] A. J. Nozik, "Quantum dot solar cells," *Physica E*, vol. 14, no. 1-2, pp. 115–120, 2002.

[92] V. I. Klimov, J. A. McGuire, R. D. Schaller, and V. I. Rupasov, "Scaling of multiexciton lifetimes in semiconductor nanocrystals," *Physical Review B*, vol. 77, no. 19, Article ID 195324, 2008.

[93] P. Gleckman, J. O'Gallagher, and R. Winston, "Concentration of sunlight to solar-surface levels using non-imaging optics," *Nature*, vol. 339, no. 6221, pp. 198–200, 1989.

[94] M. Frites and S. U. M. Khan, "Visible light active hydrogen modified (HM)-n-TiO_2 thin films for photoelectrochemical splitting of water," *Electrochemistry Communications*, vol. 11, no. 11, pp. 2257–2260, 2009.